To the Graduate Council:

I am submitting herewith a thesis written by Jere J. Matty entitled "High-Pressure, Clear-Air Ablation Measurements in the AEDC/VKF Hypervelocity Track G." I have examined the final copy of this thesis for form and content and recommend that it be accepted in partial fulfillment of the requirements for the degree of Master of Science, with a major in Mechanical Engineering.

Frank G. Collins

Frank G. Collins, Major Professor

We have read this thesis and recommend its acceptance:

R L Young

W R Lawrence

Accepted for the Council:

C W Minkel

The Graduate School

HIGH-PRESSURE, CLEAR-AIR ABLATION MEASUREMENTS IN THE AEDC/VKF HYPERVELOCITY TRACK G

A Thesis

Presented for the

Master of Science

Degree

The University of Tennessee, Knoxville

Jere J. Matty

June 1984

ACKNOWLEDGMENTS

I wish to express sincere thanks to my major professor, Dr. Frank Collins, and committee members, Dr. Robert Young and Dr. Bill Lawrence, for their guidance. In addition, thanks are due the test project engineer, Mr. Randall Watt, and his associates at Arnold Center for carrying out the tests and reducing the basic data used in the present work. Also, appreciation is extended to Messrs. Emmett Edenfield and Brad Brown for their help with the ASCC and data plots. Finally, I must mention my wife Rosemary, whose love and constant support made this work possible.

The work reported herein was accomplished at the Arnold Engineering Development Center (AEDC), Air Force Systems Command (AFSC), Arnold Air Force Station, Tennessee. Further reproduction is authorized to satisfy the needs of the U.S. Government.

ABSTRACT

The Track G version of the ABRES Shape Change Code (ASCC-G) is used to predict the surface ablation and temperature distribution as well as the bow shock shape and location for several shots in the AEDC Track G facility. The predictions are compared with data, and an explanation offered to explain the apparent overprediction of the model surface temperature. This explanation suggests that the helium environments used at the Track G image-converter stations may bias both recession and temperature data, resulting in significant deviations from the code predictions.

TABLE OF CONTENTS

LIST OF FIGURES

NOMENCLATURE

B	Bias limit
c_2	Constant in Eq. (7), cm-^{o}K
c_p	Specific heat at constant pressure, Btu/lbm-^{o}R
DEL	ASCC internal grid point spacing, in.
D_p	Distance from receding surface to a point at which the temperature drops to 10 percent of surface temperature, in.
H_o	Stagnation enthalpy, Btu/lbm
i	Integer
K	Thermal conductivity, Btu/ft-s-^{o}R
k	Physical peak-to-valley roughness element height, mils
L_a	Model axial length, in.
L_r	Model radial thickness, in.
N	Number of measurements
P'_o	Model stagnation pressure, atm
P_∞	Static pressure, atm
$Re_{\theta,TR}$	Transition Reynolds number, $\theta\rho V/\mu$
R_n	Model nose radius, in. (unablated)
S	Precision index
s	Model stagnation point recession, in.
$\dot{s}$	Model stagnation point recession rate, in./sec

T	Temperature, $^{\circ}K$
$\bar{T}$	Average temperature value, $^{\circ}K$
T_{br}	Brightness temperature, $^{\circ}K$
T_e	Boundary-layer edge temperature, $^{\circ}K$
T_i	Individual temperature measurement, $^{\circ}K$
T_w	Wall temperature, $^{\circ}K$
t	Time, sec
U	Uncertainty of temperature measurement, $^{\circ}K$
V	Velocity, ft/sec
V_{∞}	Free-stream velocity, ft/sec
α	Thermal diffusivity, ft^2/sec
β	Model internal grid point angle, deg
$\varepsilon(\lambda,T)$	Emissivity of the material at λ and T
θ	Momentum thickness, mils
λ	Wavelength, Å
μ	Viscosity, lbm/s-ft
ρ	Density, lbm/ft^3

CHAPTER I

INTRODUCTION

An area of continued interest in the aerodynamic arena is the thermophysics associated with high-speed reentry vehicles. The large heat loads produced in reentry can be dealt with either by active cooling, such as water or gas expulsion, or passively through ablation of the thermal protection material. The resultant shape change of the passively protected entry body as well as the subsequent mass loss into the free stream will affect the flow field and the aerodynamic forces on the body. Efforts to predict the ablative shape change include model testing in high-velocity ranges and application of computational aerodynamic models.

The AEDC Hypervelocity Range/Track (G) facility has been used for this type of testing in conjunction with the Acurex Corporation's Advanced Ballistic Reentry System (ABRES) Shape Change Code (ASCC). This testing has mostly been conducted with the range at atmospheric or subatmospheric conditions; however, in the past two years a requirement to test thermal protection materials at even higher pressures has become necessary.

To meet these conditions, a relatively new technique has been used which involves pressurizing the Track G facility to obtain very high model stagnation pressure during the test. The ABRES Shape Change Code has been applied in the present work as a tool to predict the shape change, bow shock shape and location, as well as surface temperature contours of a model in the Track G facility at these high pressures.

This study covers the results from the test and compares them with the code's predictions. An explanation is suggested to account for the observed differences.

CHAPTER II

TRACK G TEST

Test Unit

Track G is 1,600 ft long (see Figure 1) and consists of the following major components:

1. the model launcher, which is a two-stage, 2.5-in.-bore powder and hydrogen gas gun, 150 ft in length;
2. the 923-ft track portion, which provides model guidance through the test environment and enables recovery;
3. the 500-ft model recovery tube, which aerodynamically stops the model through the use of pressurized helium and nitrogen gas;
4. the 1,000-ft range tank, which surrounds the track section and can be pressurized or evacuated as necessary with various gases to produce the proper environment for the test;
5. the instrumentation system, which takes the laser and image-converter photographs.

The range tank is divided by bulkheads at 45 and 345 ft from the end of the launcher. The openings in the bulkheads through which the track passes are equipped with

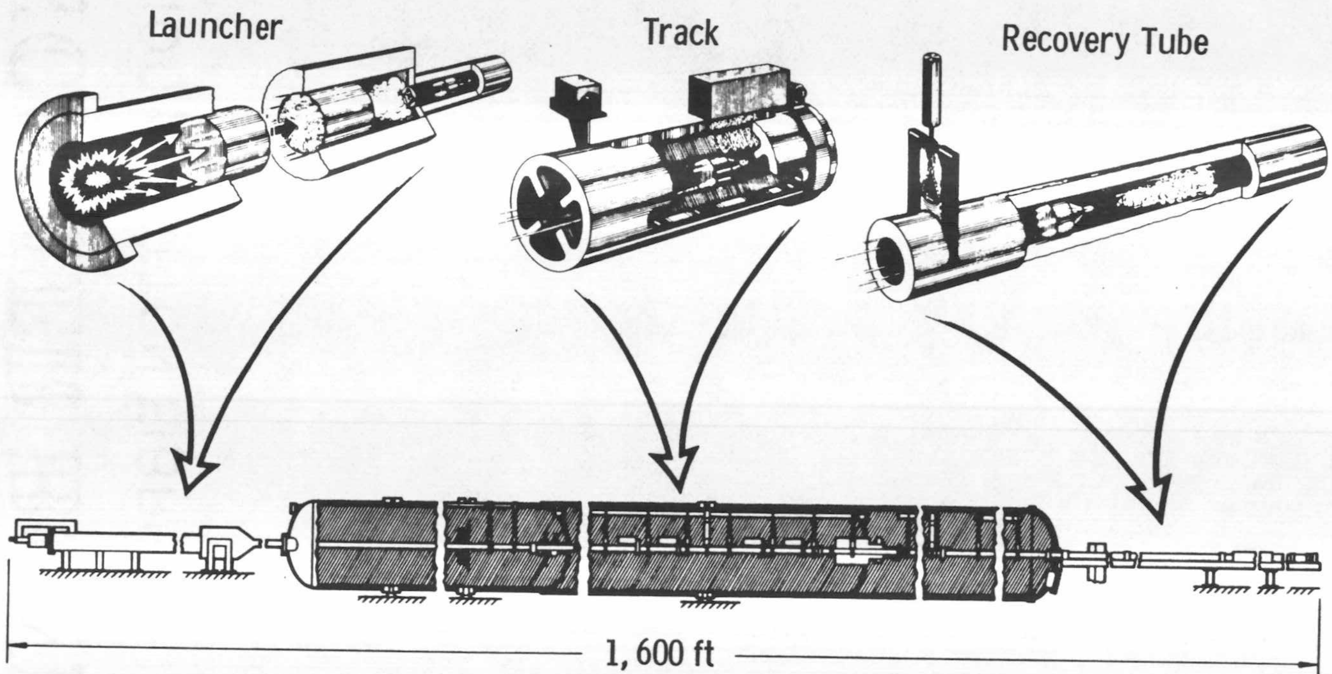

Figure 1. AEDC Hypervelocity Range/Track (G).

quick-opening valves which allow three distinct pressure levels along the range. Reference [1][1] contains a more complete description of the track system and its operation. By removing the track, the facility is also used as a free-flight range.

Instrumentation

A variety of instrumentation is used in Track G including high-speed photopyrometry and photography. Approximately six photopyrometer stations and 12 laser photography stations were located in the Track G facility to obtain data for the subject test.

Photopyrometry

A typical pyrometer station along Track G is shown in Figure 2. Two basic types of image-intensifier cameras are available. The Gen-I camera, developed in 1975, covers the temperature range from approximately 1,500 to 4,500°K, and the Gen-II camera, developed in 1976, covers the temperature range from approximately 1,200 to 2,000°K. The image-intensifier camera (IC) takes a high-speed, self-luminous photograph of the model nosetip. The same film

---

[1]Numbers in brackets refer to similarly numbered references in the Bibliography.

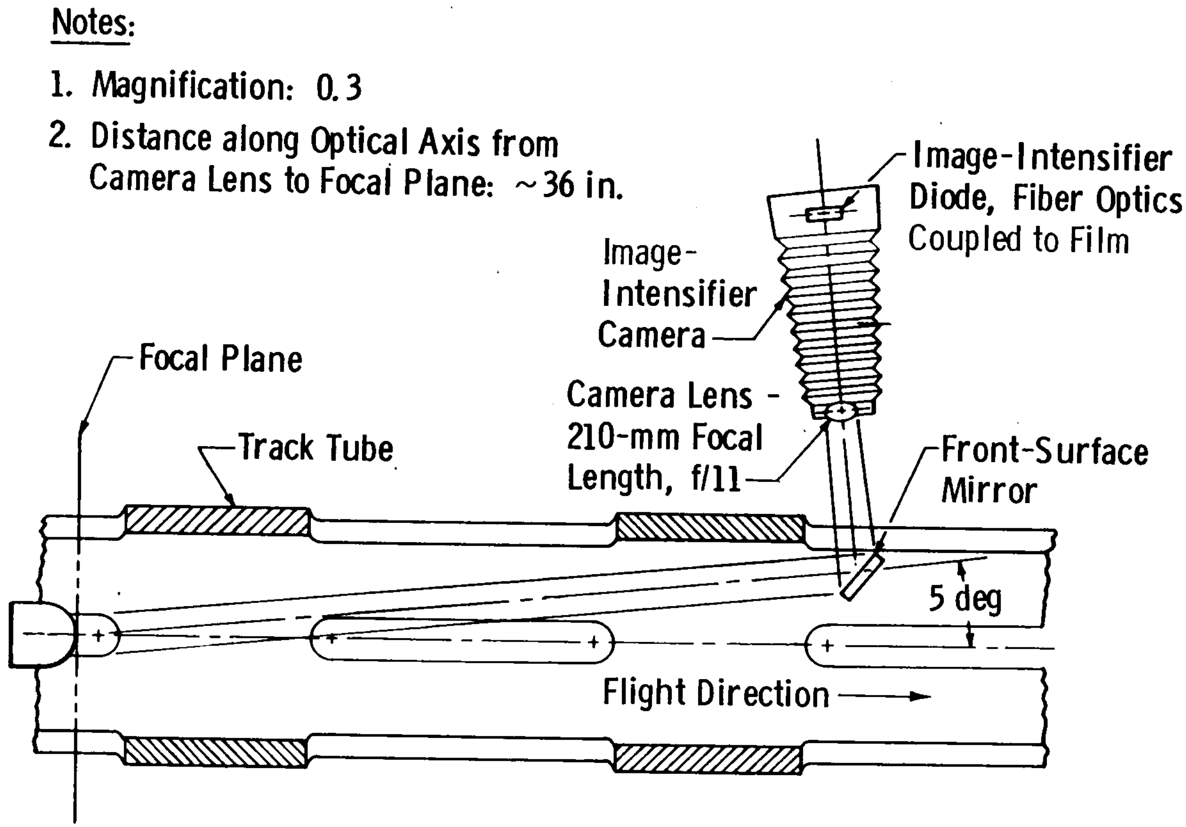

Figure 2. Track Photopyrometer Arrangement.

is exposed to a reference temperature source and processed on a high-speed, digital-scanning microdensitometer. A data reduction program then uses the reference temperature information and a density/temperature calibration curve (such as that shown in Figure 3) to produce isothermal contour maps (see Figure 4). Horizontal and vertical temperature scans of the contour maps are also produced as shown in Figure 5. This entire data acquisition and reduction process is shown schematically in Figure 6. A thorough description of the system can be found in Refs. [2] and [3].

Laser Photography

Laser photographs are taken with an open-shutter, pulsed-flash system shown schematically in Figure 7. The exposure time of 20 nsec provides high-quality, stop-motion photographs of shock shape and location as well as surface recession history.

Model Description

The model for this test series, representing the entry vehicle nosetip only, was a carbonaceous sphere cone adapted for use with the cruciform track configuration. An example model is shown in Figure 8.

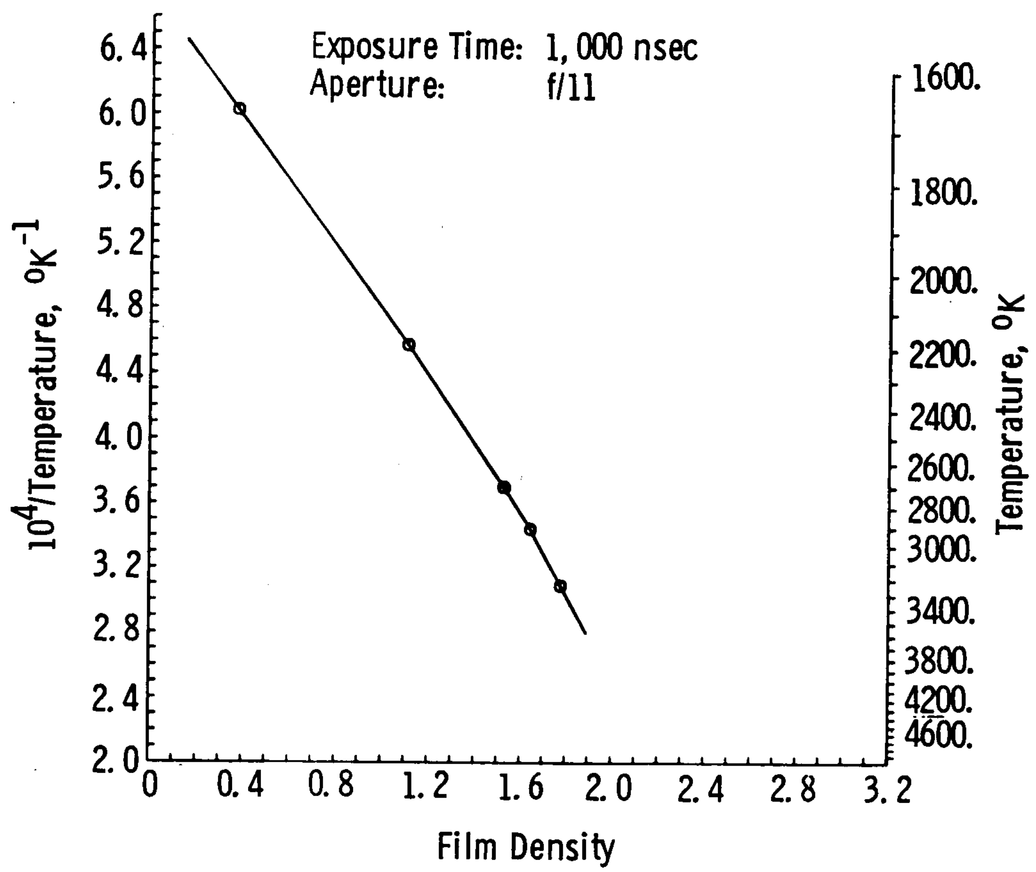

Figure 3. Photopyrometer Calibration Curve (Gen-I Photopyrometer).

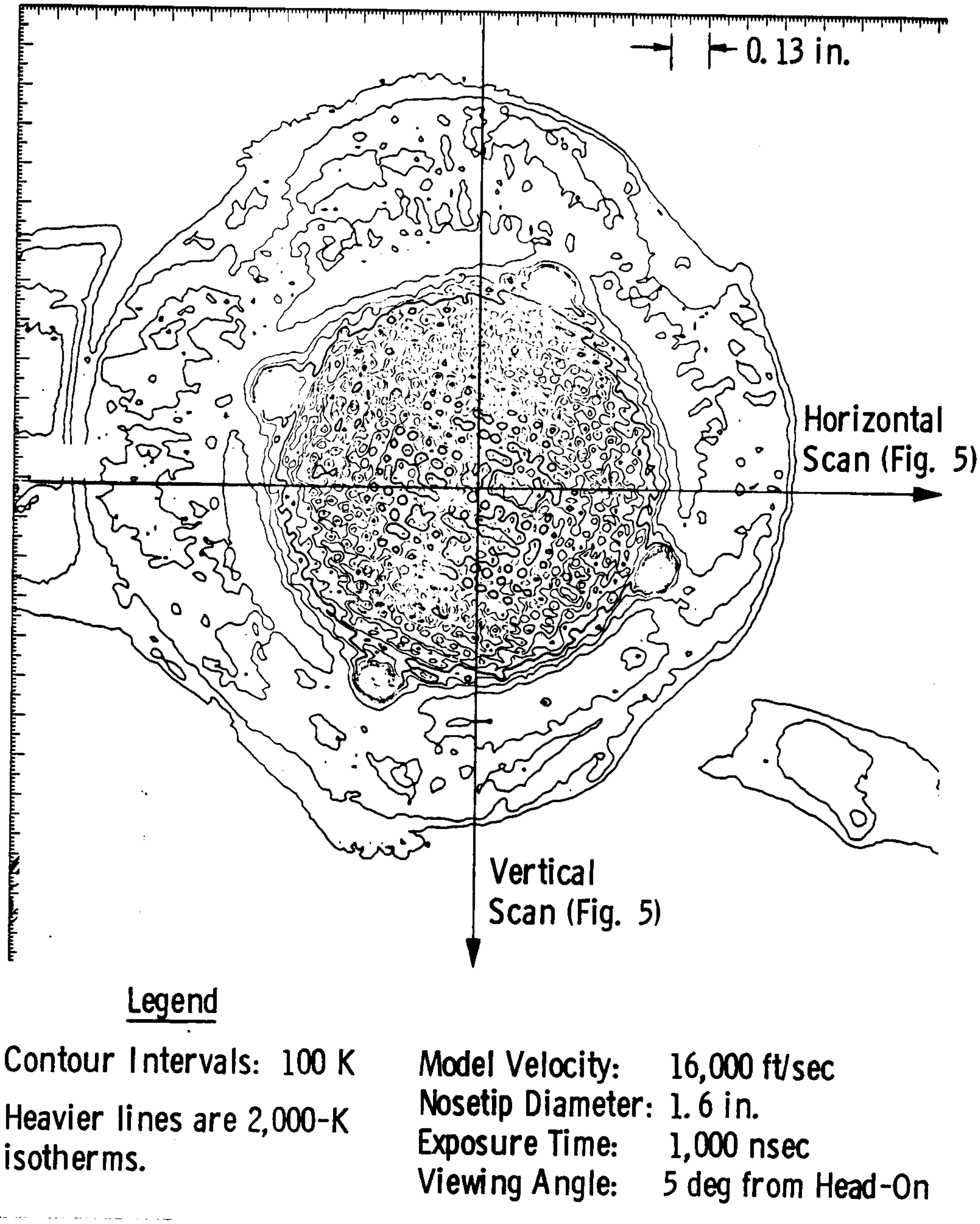

Figure 4. Isothermal Contour Map of Nosetip-Gen-I Photopyrometer.

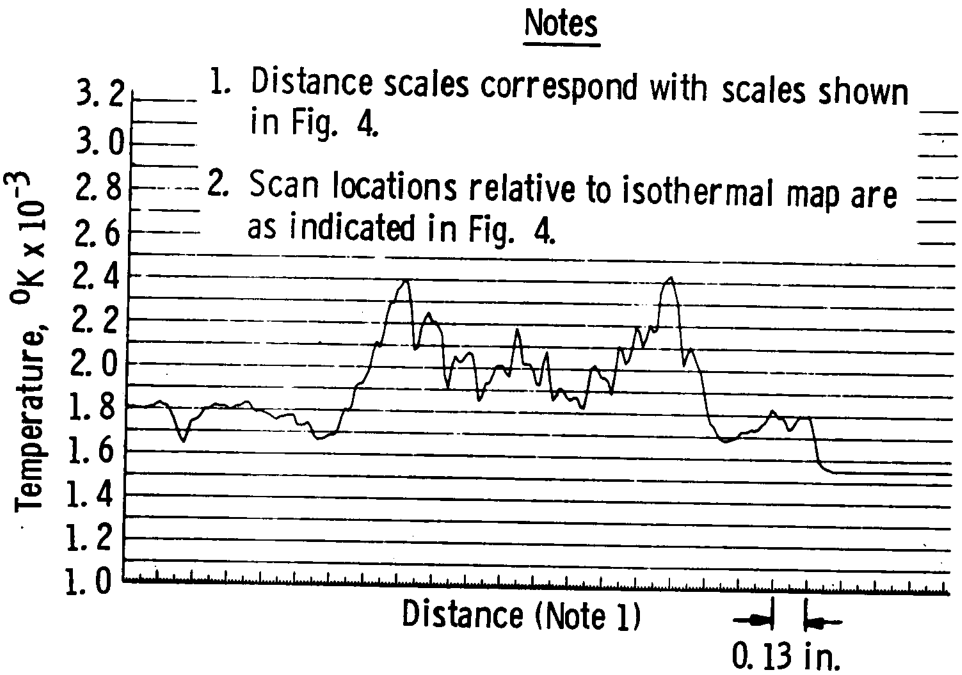

a. Horizontal Scan

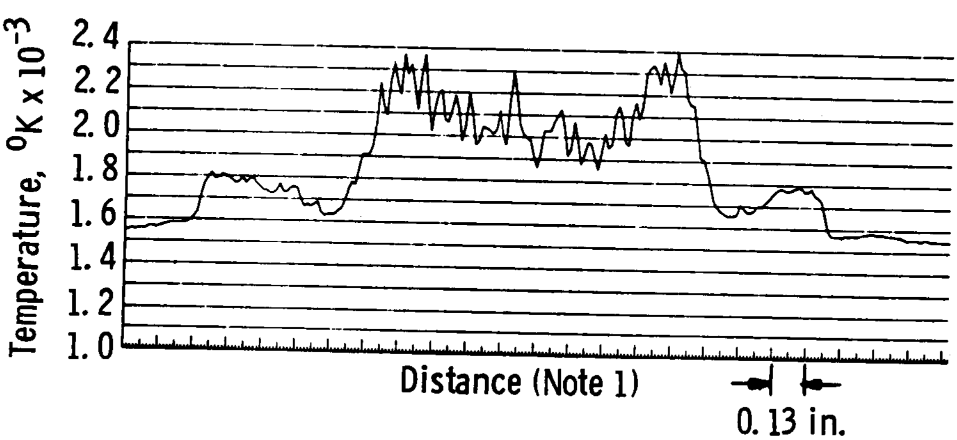

b. Vertical Scan

Figure 5. Temperature Scans Across Nosetip-Gen-I Photopyrometer.

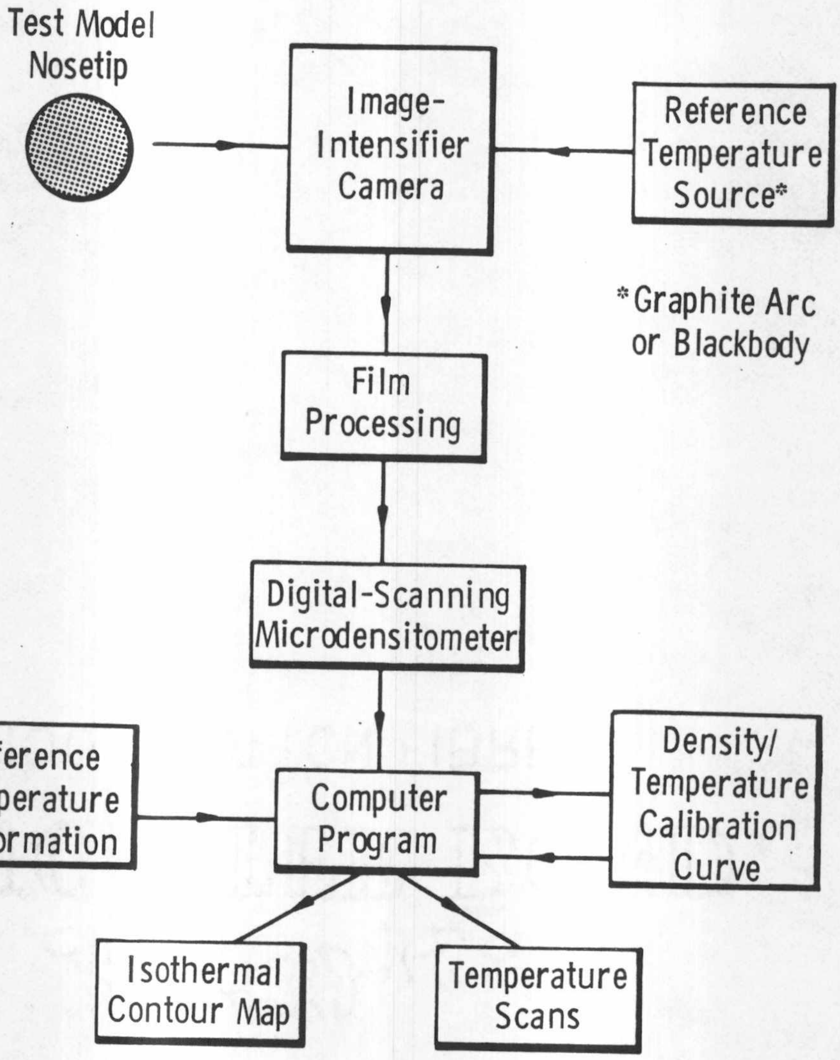

Figure 6. Data Acquisition and Reduction.

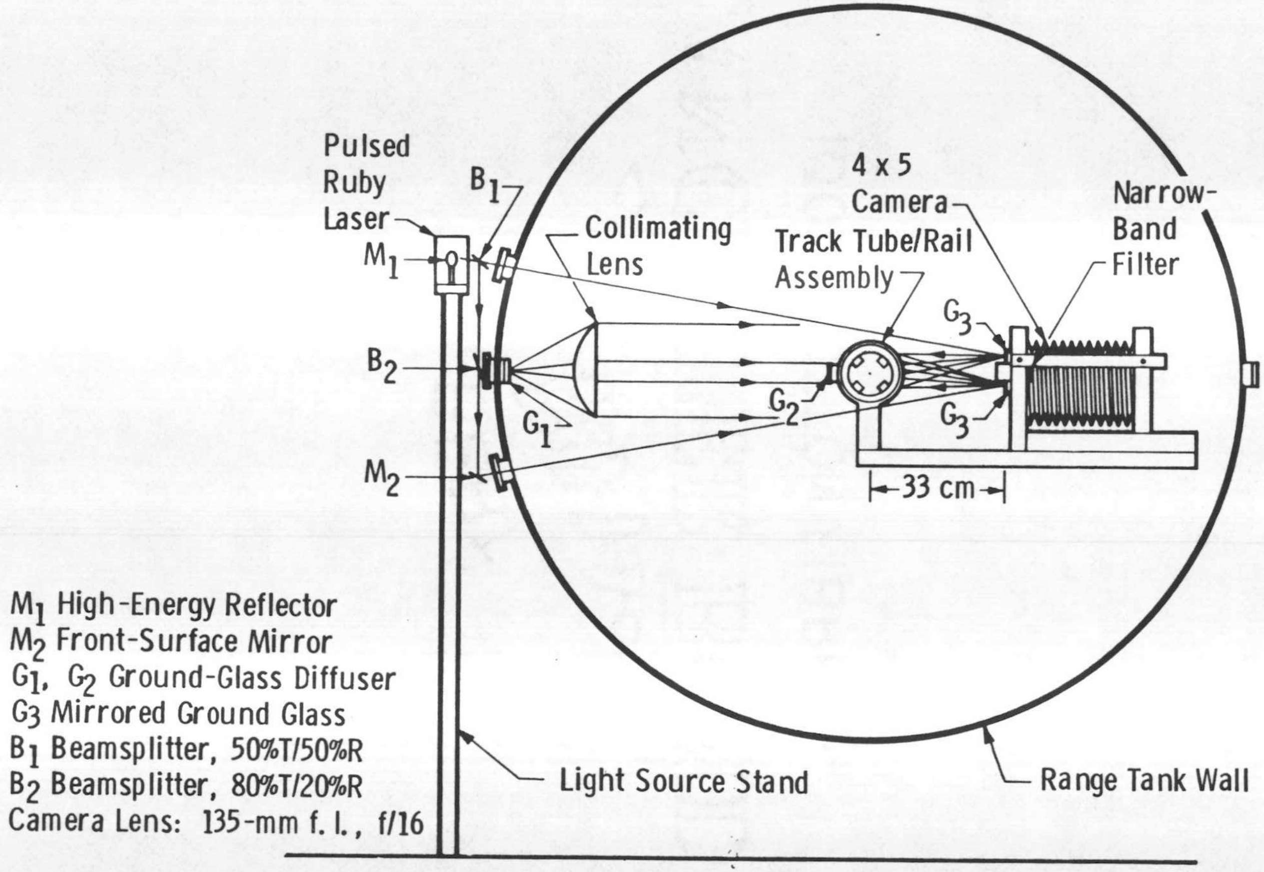

Figure 7. Track G Front-Light/Back-Light Laser Photography System.

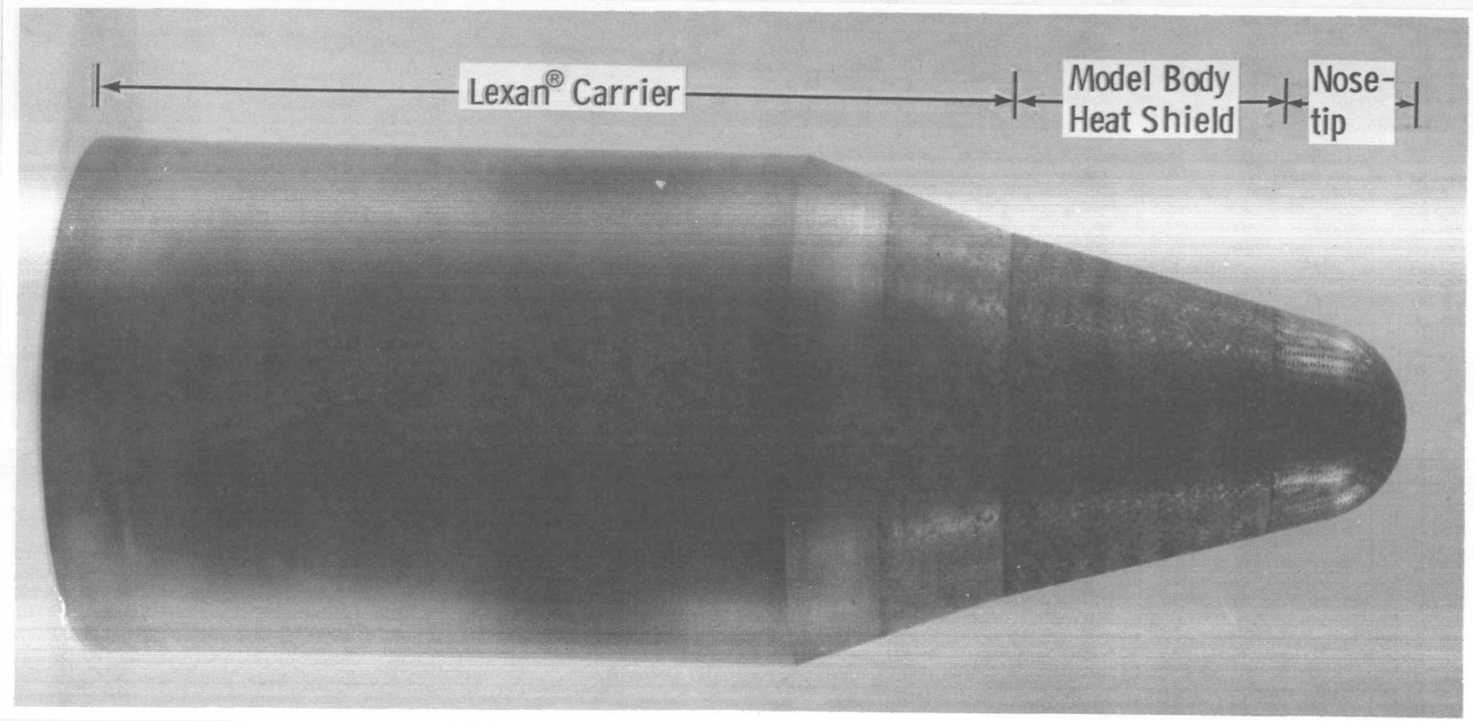

Figure 8. Typical Track G Model.

Test Procedures

The test technique used in this experiment involves launching a model along the Track G into a clear-air, high-pressure environment. The test models were launched at approximately 17,000 fps into air at a pressure of 0.4 atm for the first 300 ft, and 1.7 atm for the remaining 575 ft of the range tank. This combination of initial velocity and range pressure produced the velocity profile and stagnation properties shown in Figure 9.

Measurement Uncertainty

The two major measurement systems used in the Track G facility are the laser photographs and the image-converter cameras or photopyrometers. The recession uncertainty associated with the individual laser photograph measurement is estimated at ±3 mils. The uncertainty in the model brightness temperature distribution is a sum of the errors associated with both the pyrometer measurement system and the test article, and is described below.

Photopyrometer System Uncertainty

Although factors such as film-to-film inconsistency, film processing variations, and microdensitometer imprecision may contribute to uncertainty in the pyrometer measurement system, the major contributors are the

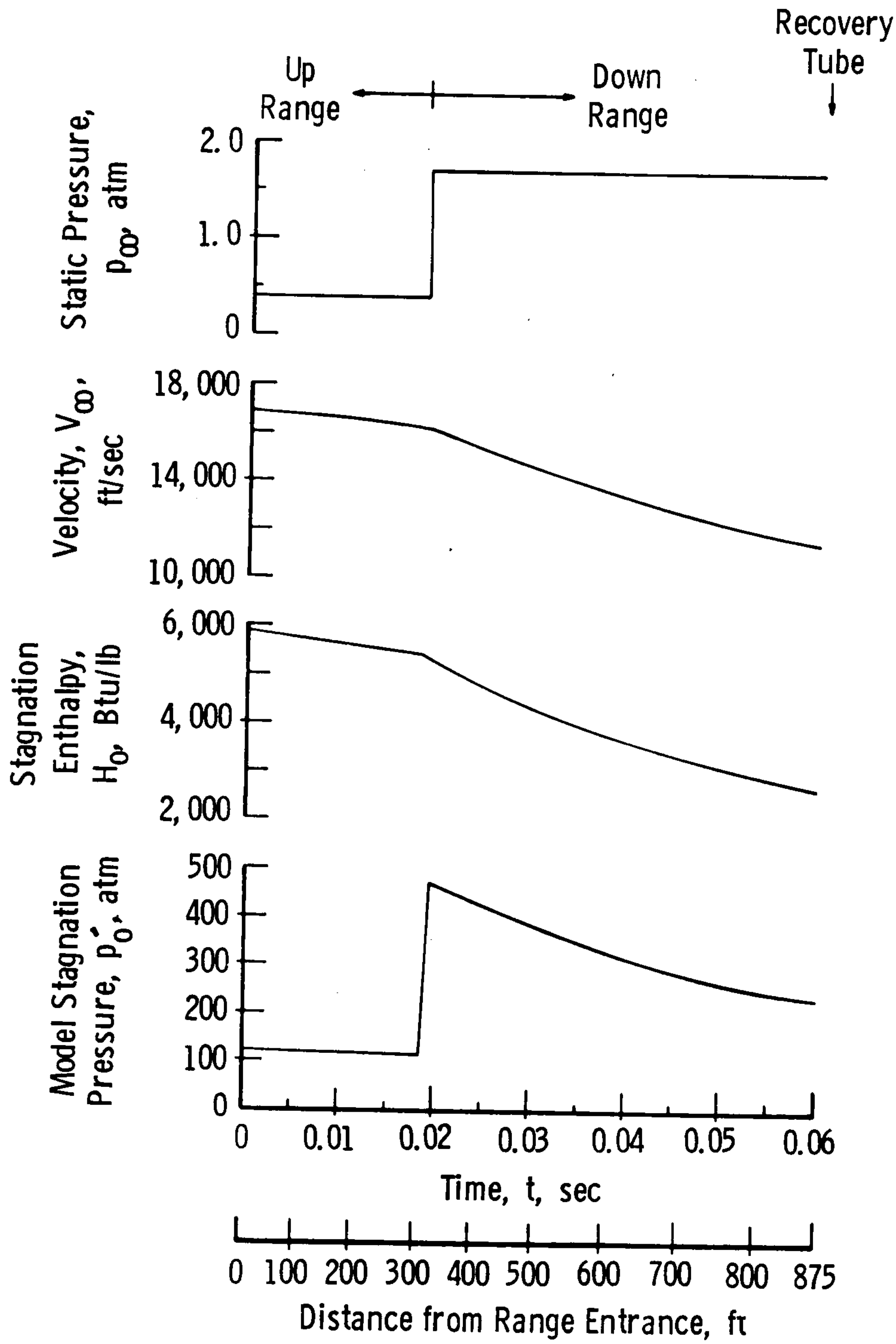

Figure 9. Test Conditions.

calibration source and the calibration curve-fit uncertainties. The calibration source uncertainty is estimated in magnitude at $\pm 15^{\circ}K$, and the error associated with using a straight line, rather than a polynomial, to curve fit the calibration data (see Figure 3, page 8) is estimated at $\pm 20^{\circ}K$. The National Bureau of Standards method for calculating the uncertainty assumes

$$U = \pm(B + t_{95}S) , \quad (1)$$

where B is the bias limit, S is the precision index, and t_{95} is the 95th percentile point for the two-tailed Student's "t" distribution [4]. The bias term, B, is calculated as simply the root sum square of the two errors listed above; that is,

$$B = \pm \sqrt{(15^{\circ}K)^2 + (20^{\circ}K)^2} \quad (2)$$

or

$$B = \pm 25^{\circ}K . \quad (3)$$

The precision index, S, which is an estimate of the standard deviation, is given by

$$S = \sqrt{\frac{\sum_{i=1}^{N} (T_i - \overline{T})^2}{N - 1}} , \quad (4)$$

where N is the number of measurements made, T_i are the individual measurements, and $\overline{T}$ is the average value. The statistical value of t_{95} is a function of N. These values are then combined in Eq. (1) to yield the values of uncertainty, U, graphed in Figure 10 as a function of temperature, the type of camera used, and the exposure time [3].

Test Article Associated Uncertainty

Uncertainty sources associated with the test article include [3]:

1. motion blur,
2. chemiluminescence,
3. shock-cap air radiation,
4. heat-shield luminosity,
5. wake radiation,
6. nosetip hot spots.

Steps have been taken to minimize these errors, including the use of helium at the photopyrometer stations described below.

In cases where the shock-cap brightness temperature exceeds the model surface temperatures, as in the subject test, a short helium gas environment is provided to reduce the shock-cap radiation level below the threshold of the photopyrometers. The gas is injected below the track just prior to the pyrometer station and provides up to

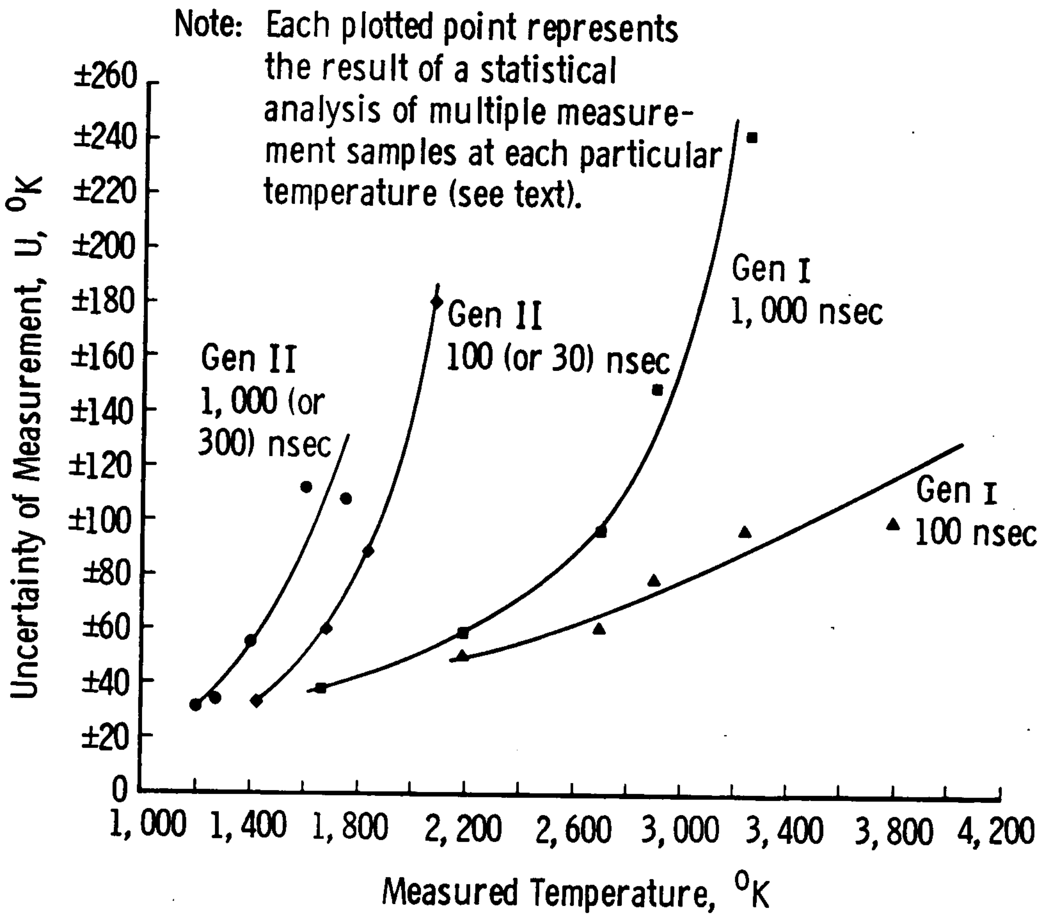

Figure 10. Photopyrometer Temperature Measurement Uncertainty.

95-percent-pure helium over a flight distance of approximately 46 in. This inert helium environment quenches, or temporarily suspends, the oxidation process which would normally result in chemiluminescence; that is, luminescence resulting from the chemical processes involved [5].

CHAPTER III

THEORETICAL MODEL

Description

The theoretical model used to predict the shape change, bow shock shape and location, and surface temperature data from the present test is the Track G version of the ABRES Shape Change Code (ASCC-G). The main inputs to the code are the material properties, the model configuration, the free-stream conditions, and the model velocity-time history. The major computational elements of the code that are used in the present analysis are the inviscid solution, viscous solution, surface mass/energy balance, and in-depth transient heat conduction. The resultant shape change, in-depth temperatures, and flow-field characteristics are calculated as the program moves forward in time (see Figure 11).

The inviscid calculations are made by dividing the nosetip into three regions: (a) stagnation point to sonic point; (b) sonic point to aft shoulder; and (c) aft shoulder to the end of the nosetip. The surface pressure ratio is then calculated over each region using semi-empirical relationships. The viscous portion of the code uses a simultaneous solution of the momentum/energy

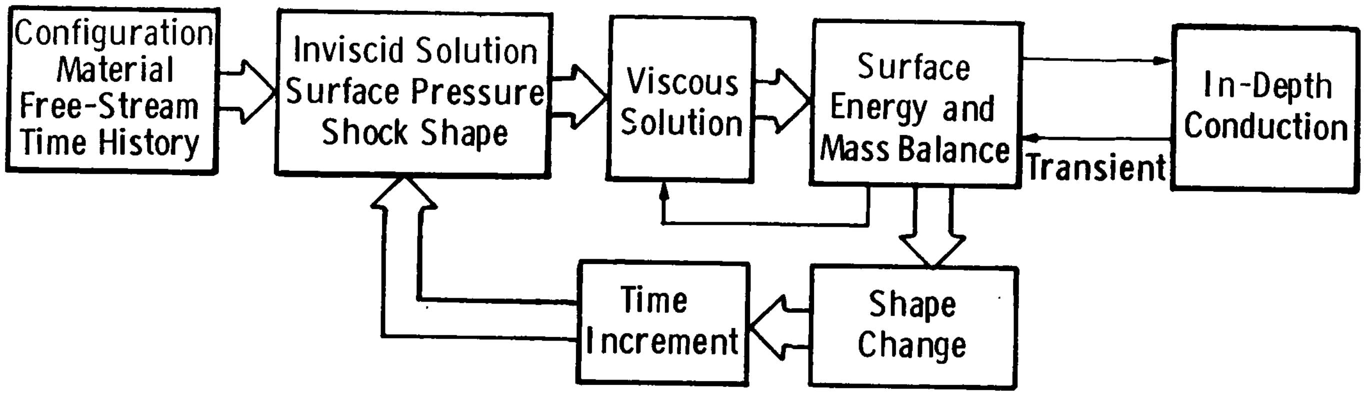

Figure 11. ASCC Computational Elements.

integral equations modified for the reentry vehicle conditions through the use of influence coefficients. These coefficients account for flow acceleration, surface roughness, and transition proximity.

The surface energy balance is computed between the following: (a) sensible convective heat flux; (b) chemical energy flux; (c) radiative heat flux; (d) energy attributable to movement of the control volume into the model; and (e) conduction heat flux (see Figure 12).

A more complete description of the basic ASCC code, 1976 version, is found in Ref. [6].

Theoretical Model Application

The first step in applying the theoretical model is laying out the computational mesh. The fixed polar coordinates cover the flow-field computational area, and the internal grid points cover the test article (see Figure 13). The depth to be covered by the internal grid point layout was calculated through the use of a steady-state analysis of a semi-infinite solid with constant surface heat flux and recession rate as follows:

$$D_p = \frac{2.3\alpha}{\dot{s}} \tag{5}$$

and

$$\alpha = \frac{k}{\rho c_p} , \tag{6}$$

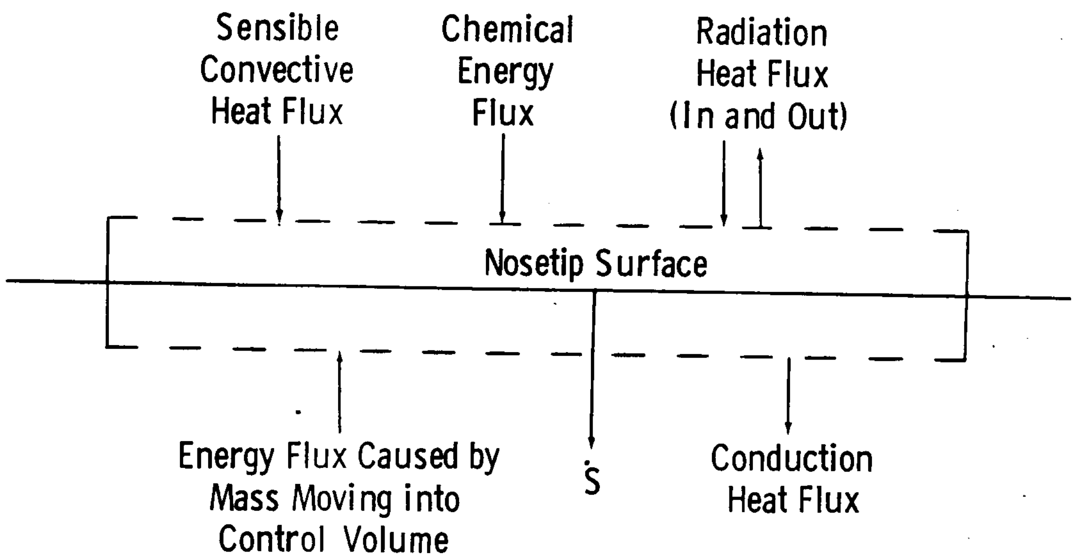

Figure 12. ASCC Surface Energy Balance.

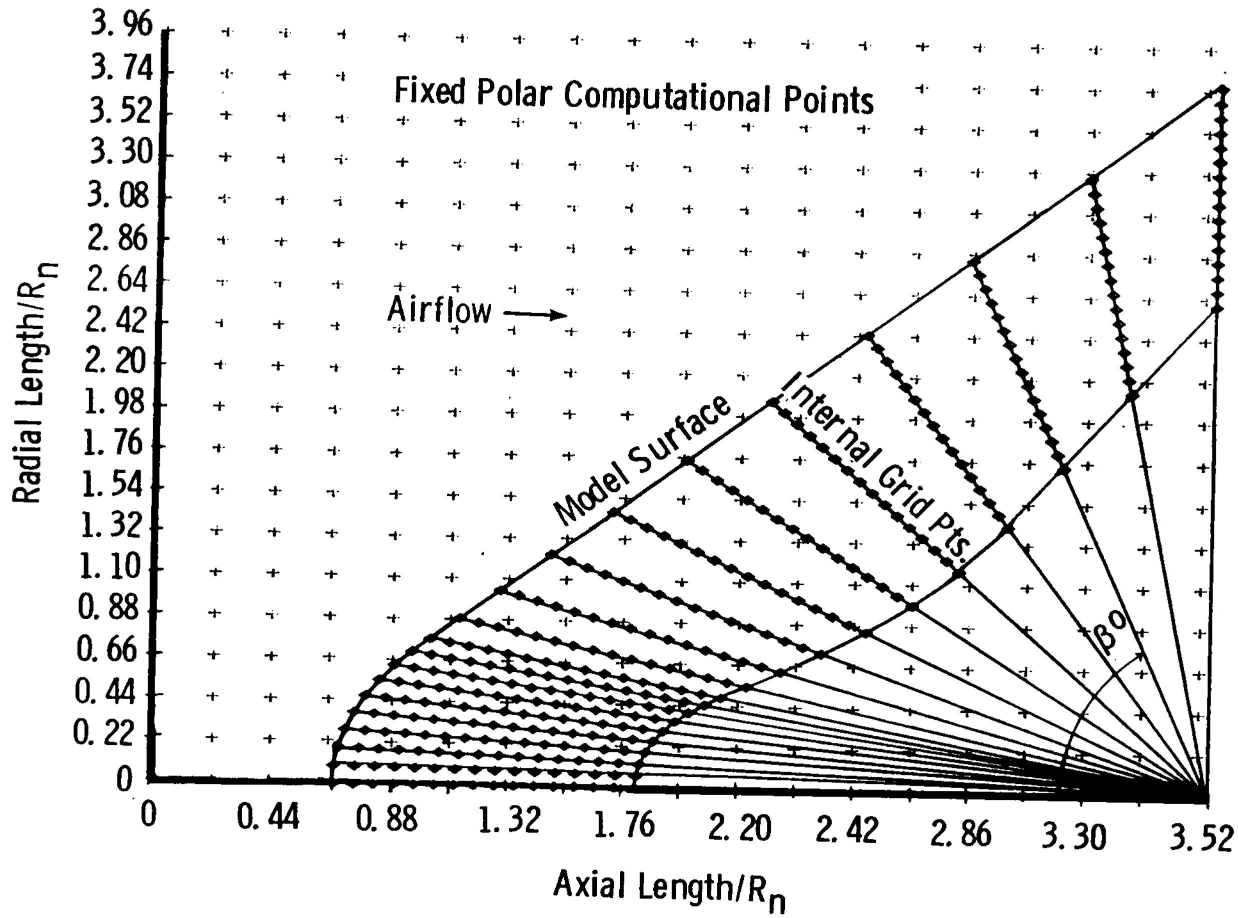

Figure 13. ASCC Computational Grid Layout.

where α is the material thermal diffusivity, k is the thermal conductivity, ρ the density, c_p the specific heat at constant pressure, and D_p the distance from the receding surface to the point within the model where the temperature drops to 10 percent of the surface temperature. Acceptable layouts were achieved for both the fixed polar and the internal grid point systems.

Several options are available within the code to handle the boundary-layer transition. The decision to use the code's abrupt turbulent-boundary-layer input option, which assumes a turbulent boundary layer throughout the run, was based on correlations of previous ballistic range experiments by Reda [7]. Figure 14 depicts the general approach used in his correlations.

Figure 15 shows the correlation applicable to the ballistic range data for various carbonaceous materials. Calculations of $Re_{\theta,TR}$ for the case in point were well into the turbulent region regardless of which correlation was employed in Figure 15. The surface thermochemistry tables input into the ASCC-G were generated by the Aerotherm Chemical Equilibrium (ACE) program [8].

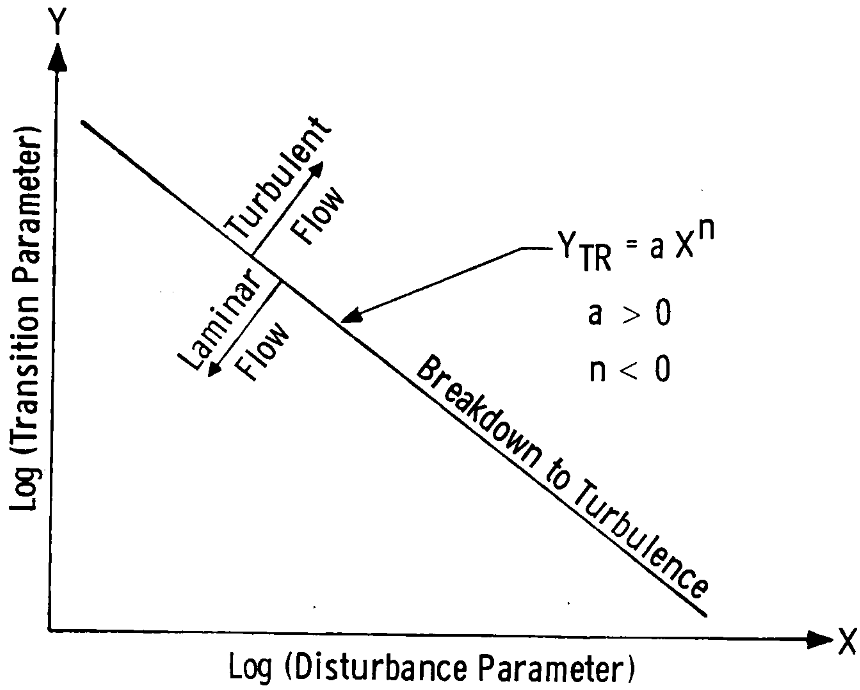

Figure 14. Generalized Correlation Approach Applied to Nosetip-Transition Data [7].

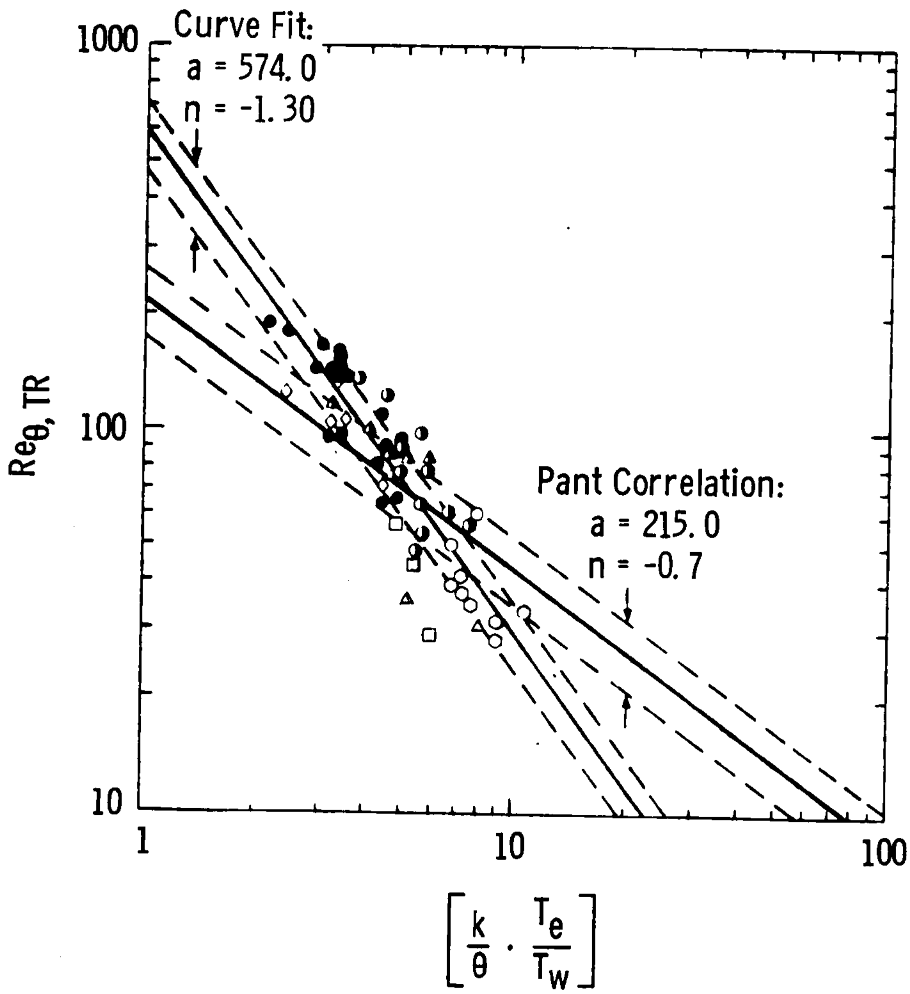

Figure 15. Ballistics-Range Data versus PANT Correlation [7].

CHAPTER IV

EXPERIMENTAL/THEORETICAL RESULTS

The measurable parameters from the test were compared with the ASCC-G predictions and include bow shock shape and location, stagnation point recession, and model brightness temperature profiles. Over 30 high-pressure, ablation shots have been conducted in Track G. Of these, the largest group, with almost identical model configurations and test conditions, contained six shots. Although the comparisons were completed on each of these shots, only a representative shot is presented here.

Bow Shock Shape and Location

Bow shock shape and location were read directly from the laser photographs. A typical example is shown in Figure 16. To avoid the problem of having the code predict a shock on a predicted model shape, the actual ablated model profile at a given laser station was digitized, input into the ASCC-G, and "frozen" by selecting a no-shape-change option. The code predicted the shock shape and location at the appropriate laser station (see Figure 17). The prediction agrees well with the data with the exception of the area near the nosetip which may be due to the coarse

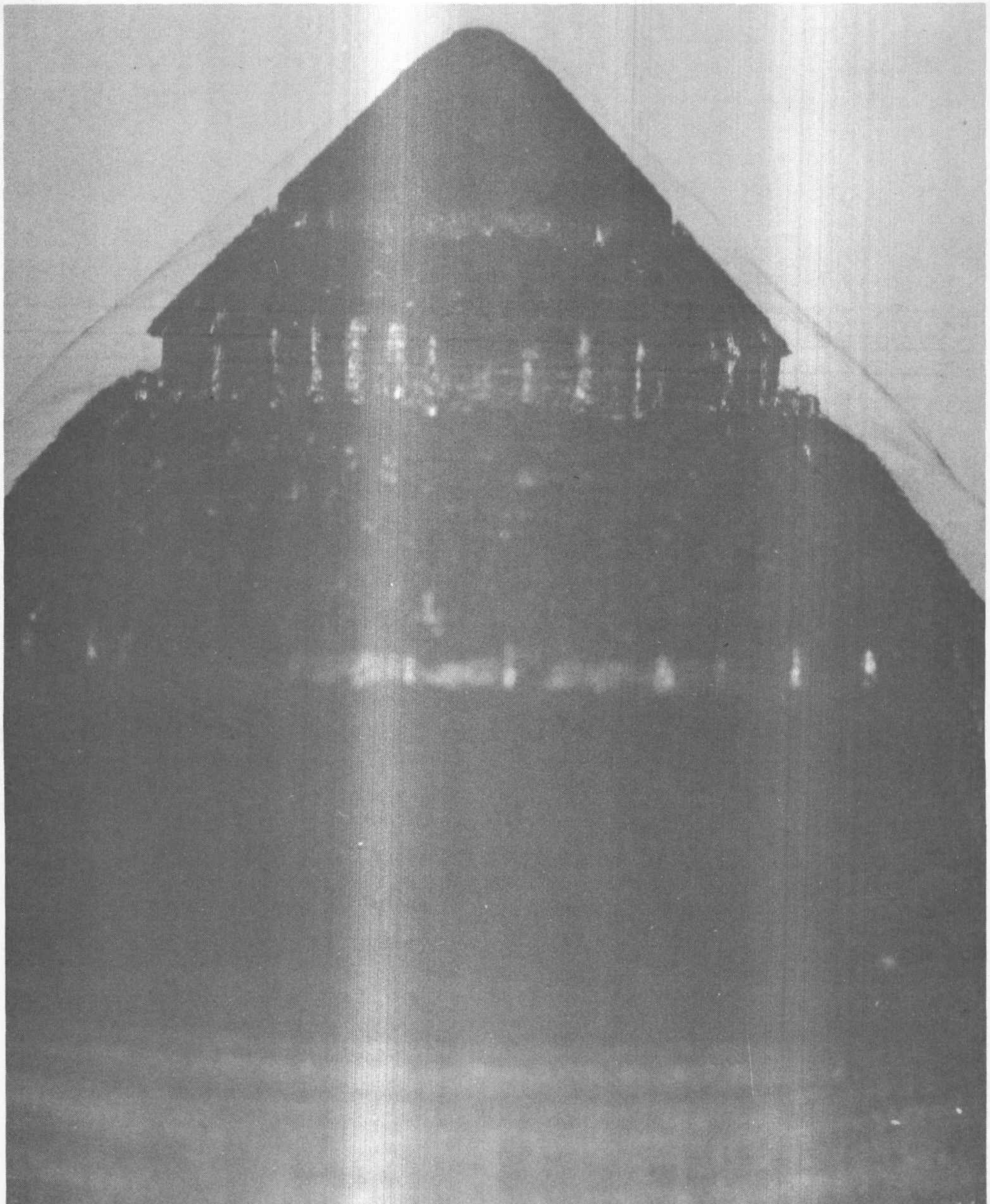

Figure 16. Typical Track G Laser Photograph.

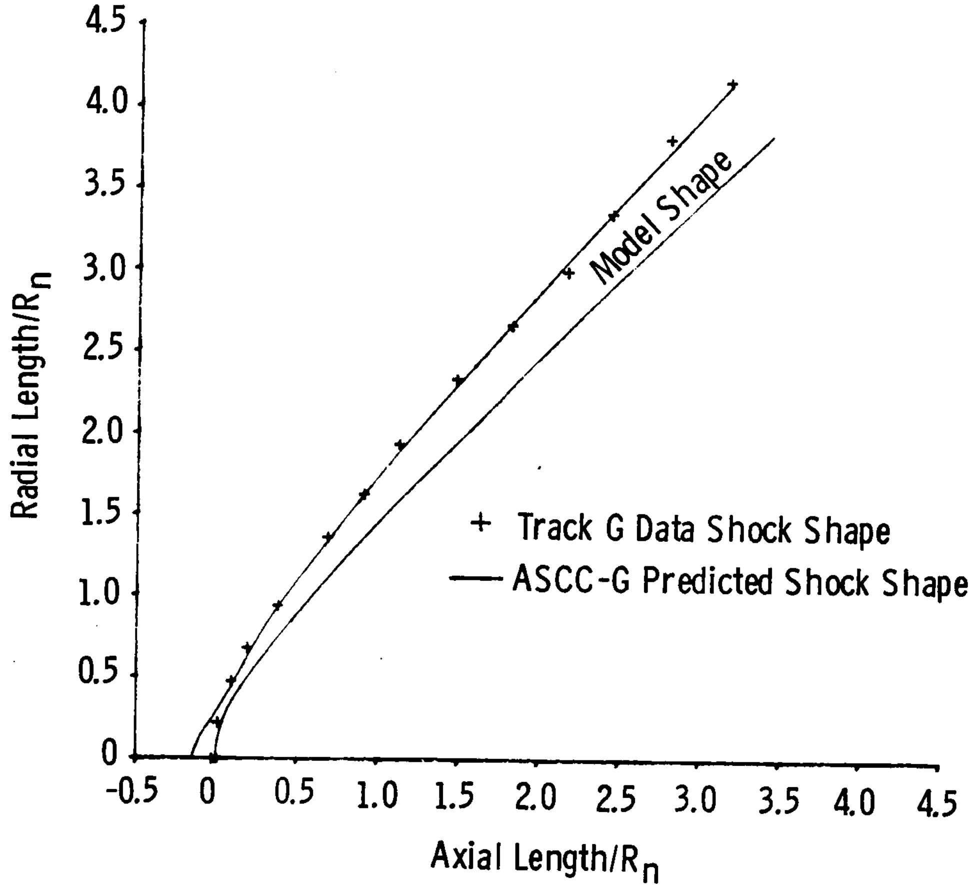

Figure 17. Bow Shock Shape and Location versus Theory.

computational grid layout relative to rapid changes in the flow field in that area. Because of the nature of the code, when an exact model profile is input, as in this case, the code lays out the computational grids automatically with no provisions for variation as were made in the following stagnation point recession calculations.

Stagnation Point Recession

The stagnation point recession data from the laser photographs are compared to the ASCC-G predictions in Figure 18. Even though the curves show similar trends, the prediction is consistently below the data. Hence, checks were made on the internal grid point spacing. Calculations using 2, 2.5, and 3 times the calculated minimum required spacing yielded little change (see Figure 19). The solution's insensitivity to grid changes suggests a proper grid layout. More will be said about the difference noted here between theory and data in the discussion of the model surface temperature measurements.

Model Brightness Temperatures

The high-speed image-converter photographs produce model brightness temperature, T_{br}, profiles. This brightness temperature is related to the actual model surface temperature, T, by the following relation which is derived

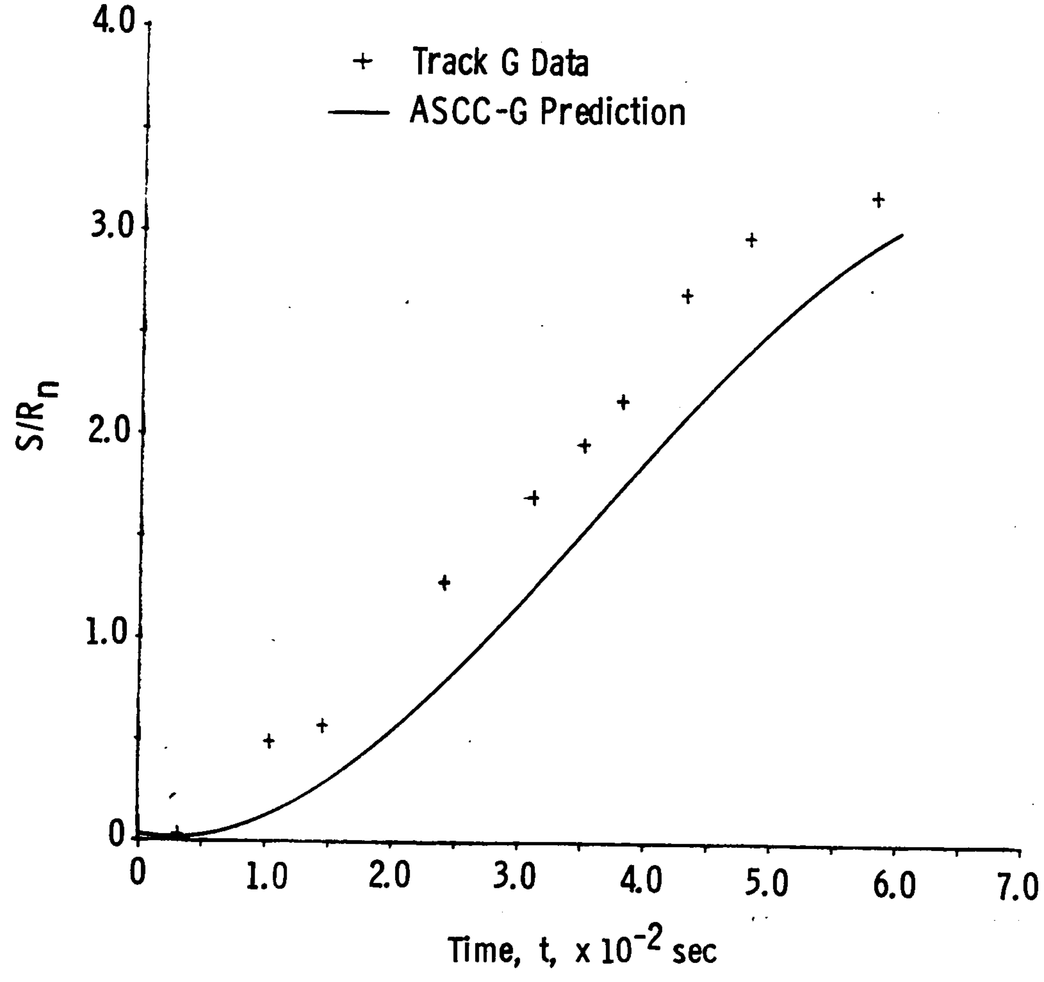

Figure 18. Stagnation Point Recession versus Theory.

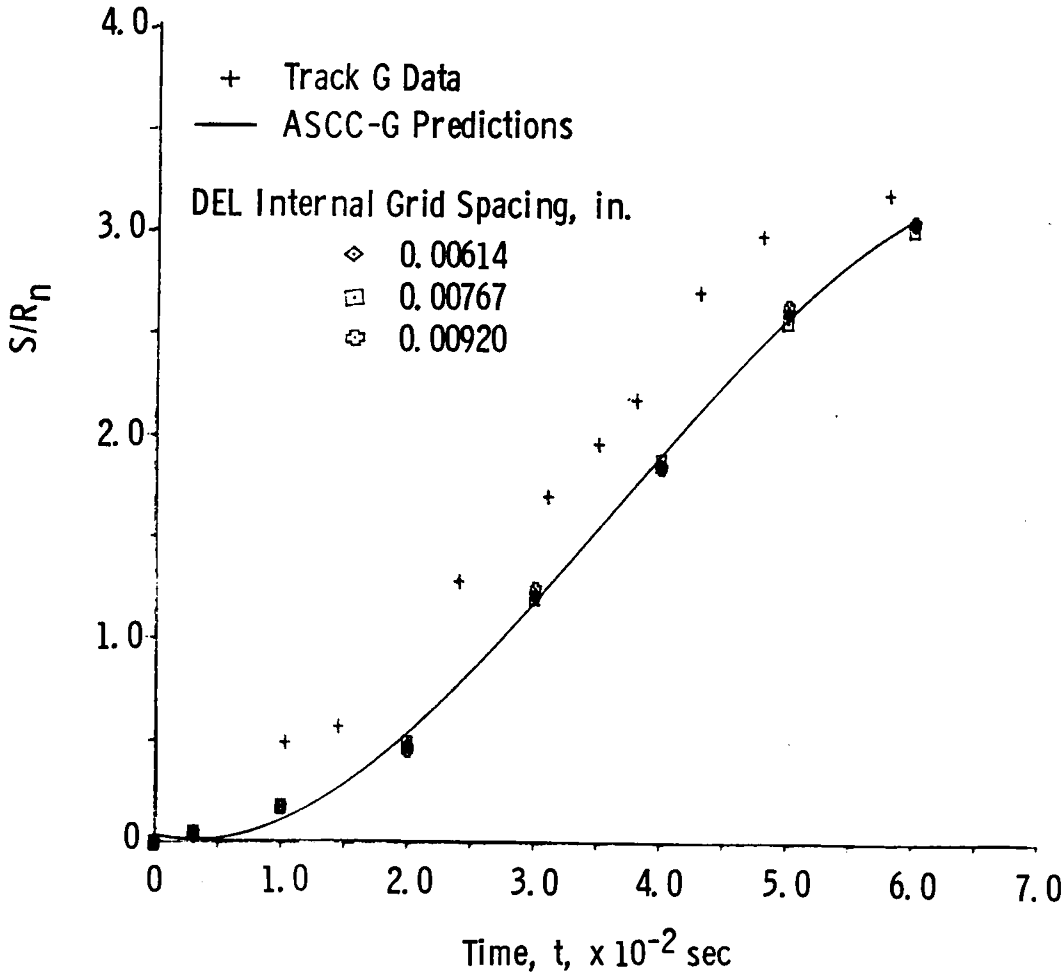

Figure 19. Stagnation Point Recession versus Theory (with Varied Grid Point Spacing).

from Planck's formula:

$$\ln \varepsilon(\lambda,T) = \frac{c_2}{\lambda}\left(\frac{1}{T} - \frac{1}{T_{br}}\right) , \quad (7)$$

where c_2=1.4350 cm-$^{\circ}$K (international temperature scale of 1948) [9]. For the pyrometers used in the Track G facility, a typical spectral response curve is shown in Figure 20 and ranges between 5,300 and 9,000 Å. The emissivity of the test material is assumed constant with respect to the wavelength and temperature. With an emissivity value of 1.0, the brightness temperature is equal to the surface temperature by Eq. (7). Figure 21 shows the possible differences between the brightness temperature and the surface temperature, ΔT, as a function of emissivity. Note that there is very little temperature deviation between the extremes of the pyrometer response wavelengths such that, if the actual material emissivity varies from 1.0, the effect on the relationship between the brightness and to true temperature is relatively small.

The profile of model brightness temperature as measured by the image-converter cameras is circumferentially averaged and presented in terms of degrees Beta, where 0° corresponds to the model stagnation point (see Figure 13, page 24). The results are shown in Figures 22 and 23 for two data stations spaced 300 ft apart. The

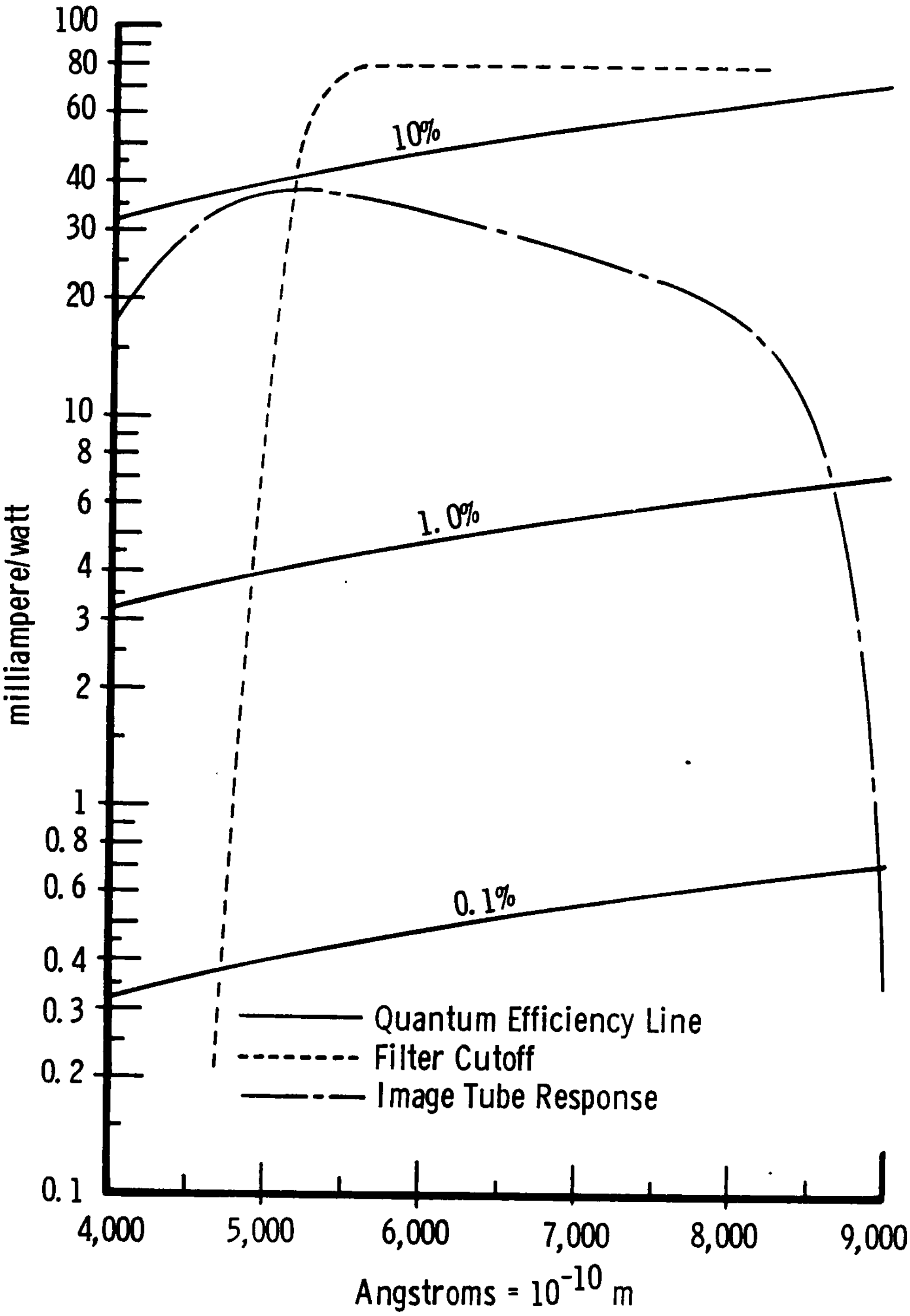

Figure 20. Typical Track G Pyrometer Spectral Response Curve.

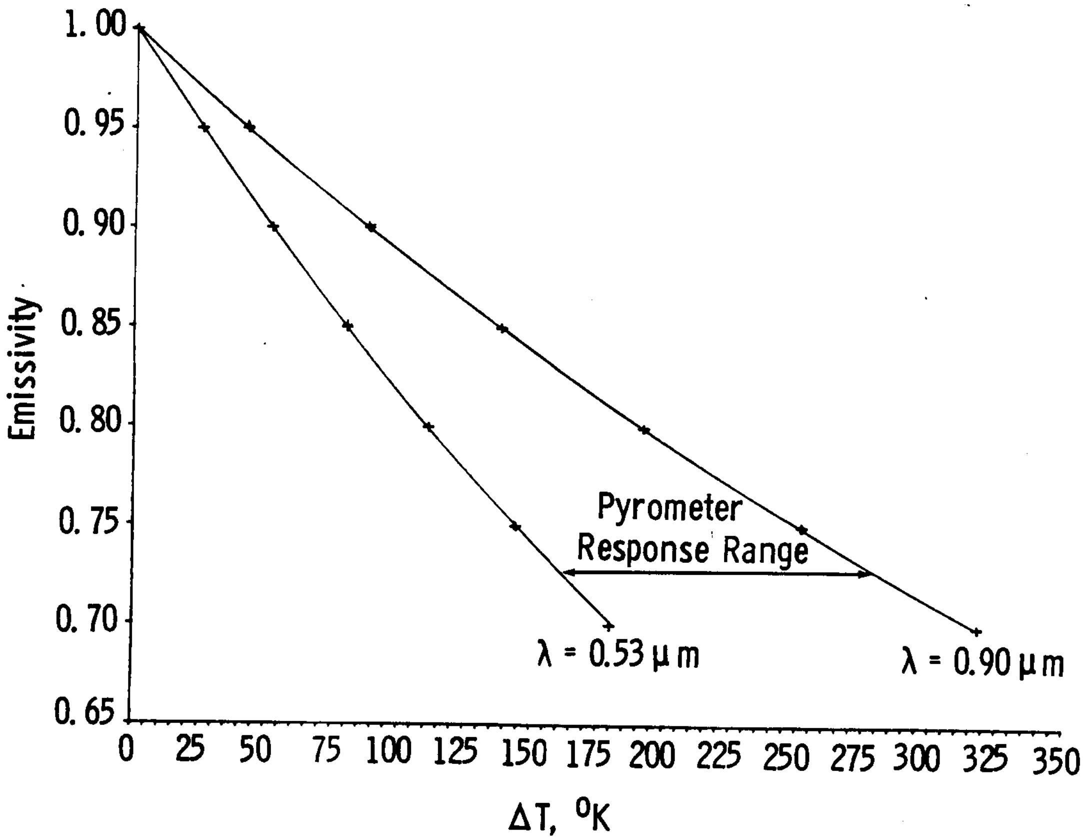

Figure 21. Emissivity Effect on Brightness Temperature to True Temperature Conversion.

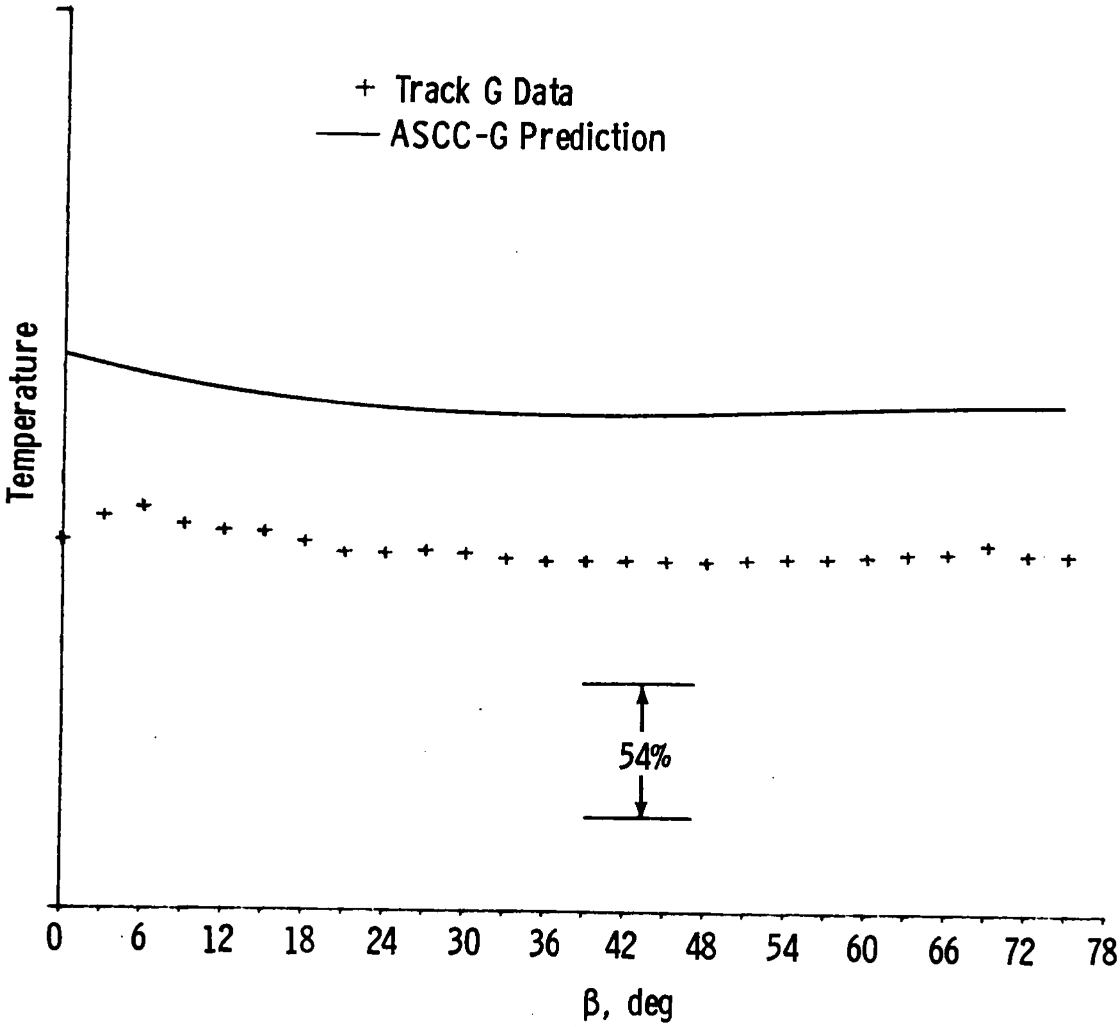

Figure 22. Circumferentially Averaged Surface Temperature versus Theory (IC 4).

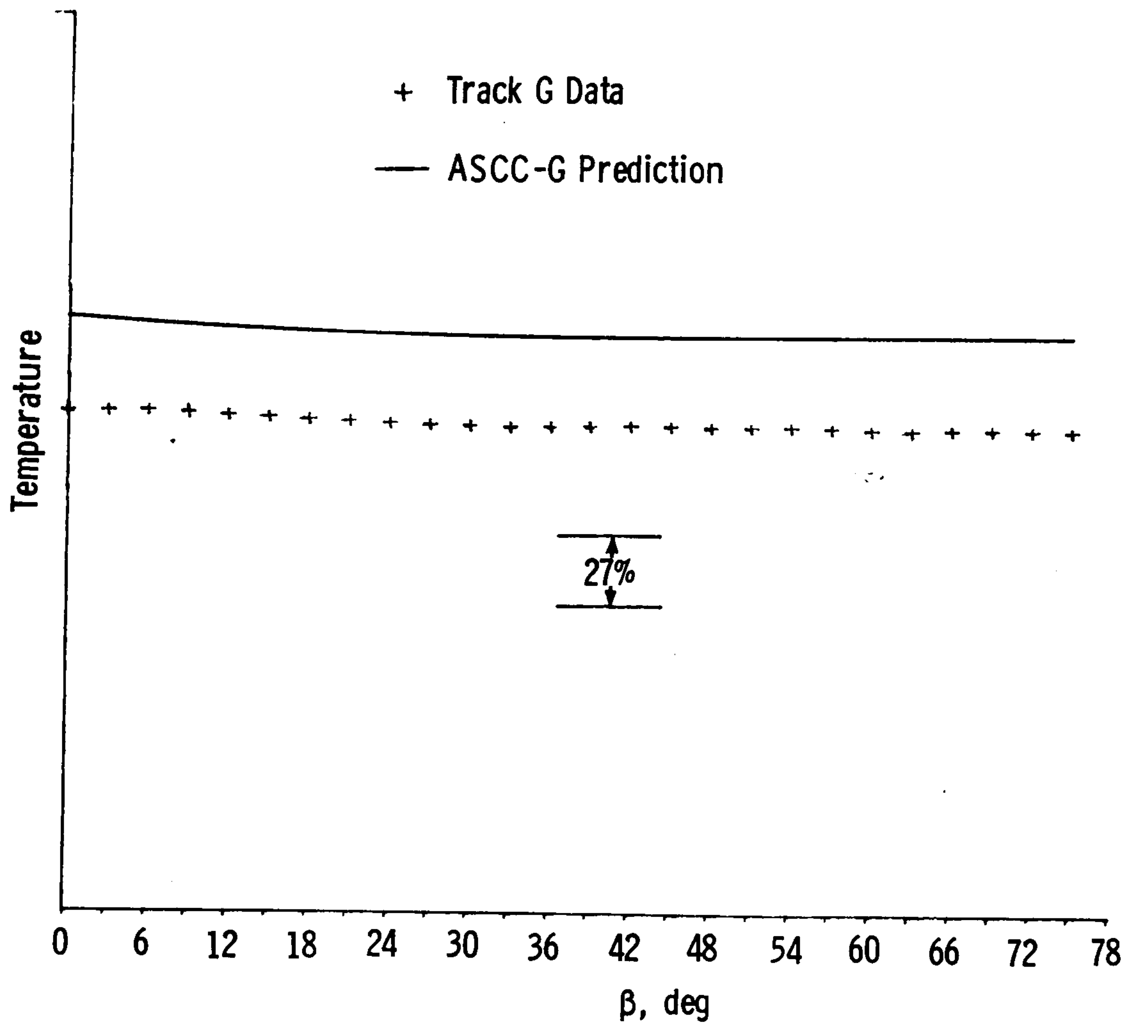

Figure 23. Circumferentially Averaged Surface Temperature versus Theory (IC 20).

emissivity of the nosetip material is assumed to be unity. In both cases, the theoretical prediction is well above the data.

To check proper code usage, the prediction of the stagnation temperatures for several low-pressure shots were made with good results as shown in Figure 24. The following avenues were explored to account for the apparent discrepancy in the high-pressure predictions:

1. possible errors resulting from stagnation point identification during data reduction;
2. alterations to the data reduction algorithm to account for exact model shape;
3. improper chemical modeling within the code;
4. possible data biasing by the helium shock-cap quench technique used in conjunction with the temperature measurement system.

The stagnation point is located manually during the data reduction process and provides the reference point for all other temperature measurements. In an attempt to reduce any repeatability errors associated with this process, the surface stagnation point temperature was averaged over areas enclosed by radii from 0.050 to 0.10 in., with very little effect (see Figure 25).

The isothermal contour maps produced by the surface-temperature data reduction program had been

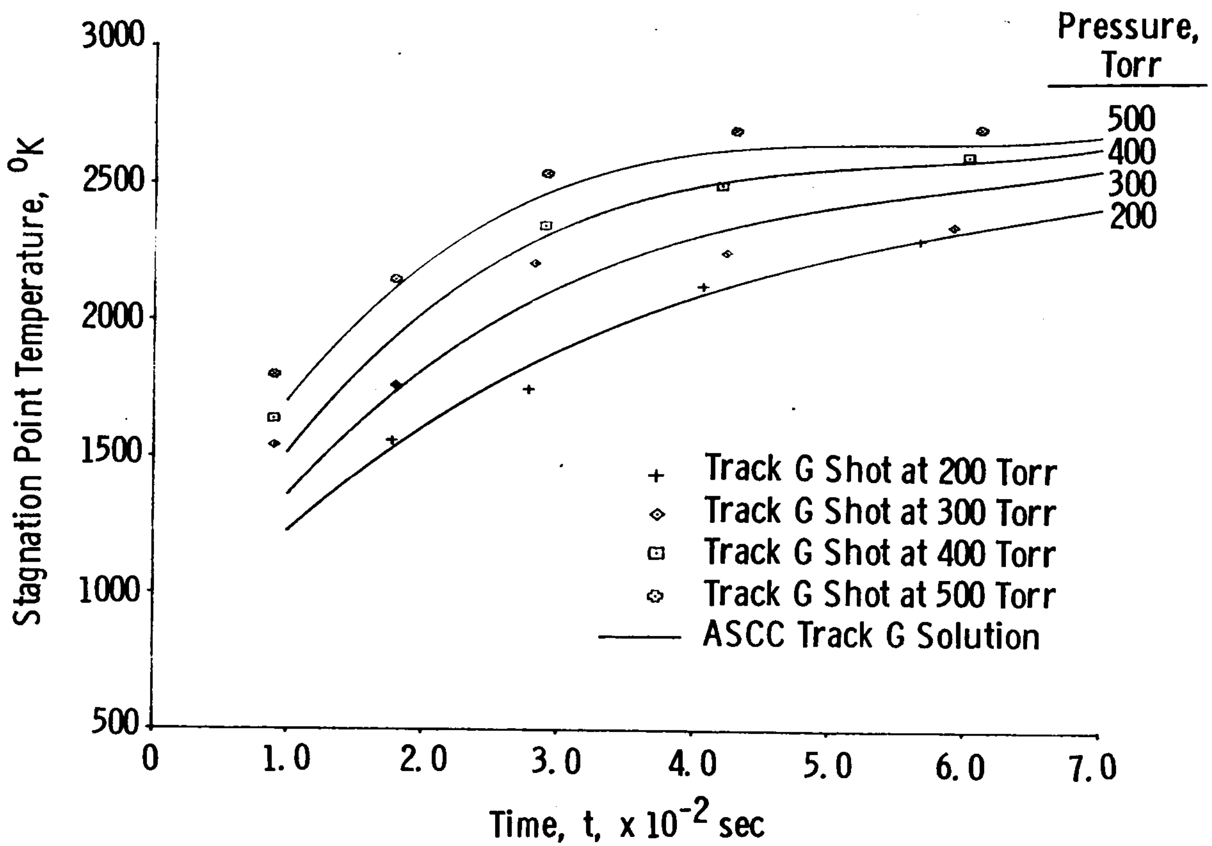

Figure 24. ASCC-G Predictions of Low-Pressure Stagnation Temperatures.

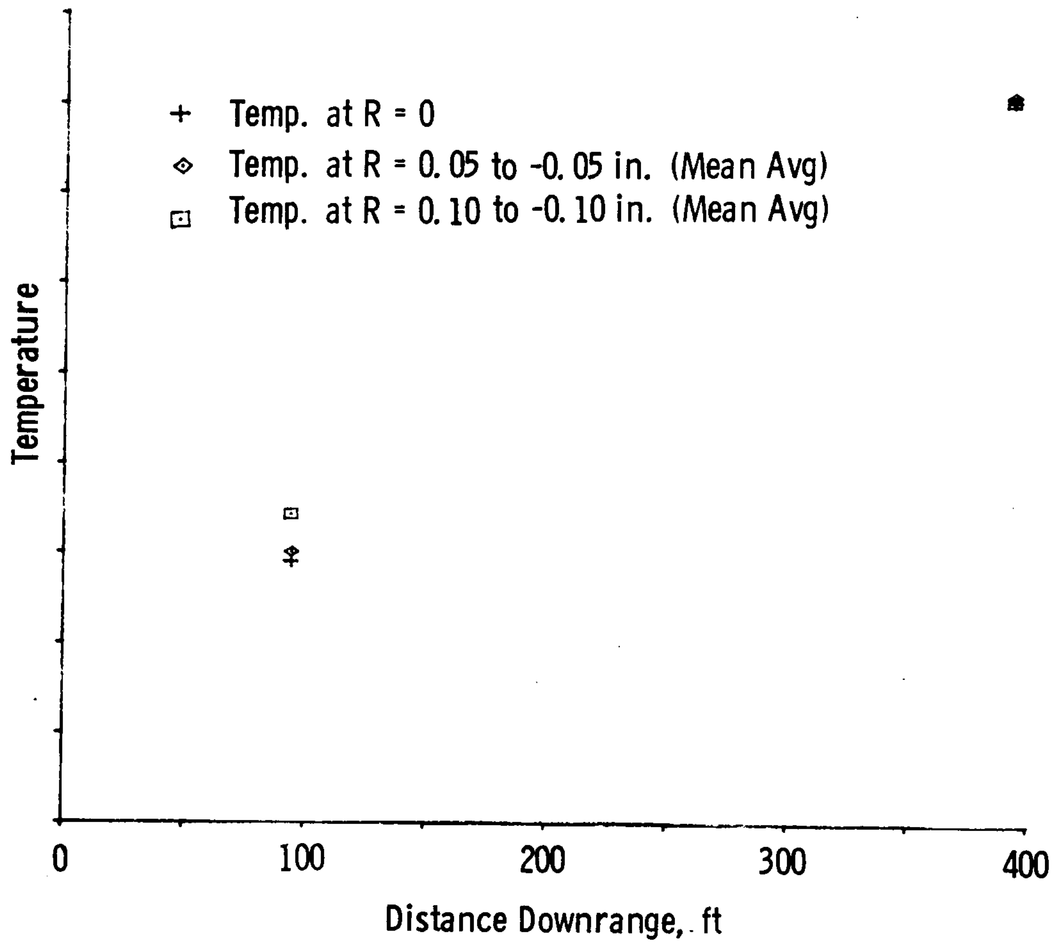

Figure 25. Effect on Temperature of Averaging the Stagnation Point Location.

designed originally for cut-sphere nosetips. The program was modified to account for the sphere-cone configuration of the present model with very little effect, as shown in Figure 26.

Another possible explanation for the data-theory mismatch relates to the material thermochemical properties input into the code. These may not apply at the temperatures and pressures encountered during this test. This possibility was explored by Kratsch et al. [10], who concluded that stagnation pressures as low as 100 atm can produce an experimental mass flux from a carbon model that is about a factor of two greater than predicted by thermochemical erosion alone. Surprisingly, Kratsch noted that this increased mass loss resulted in a rather small decrease in surface temperatures.

Another area investigated was the possible effect of the helium gas used to quench the shock cap. This possibility has also been suggested by Park [11] (NASA Ames Research Center) concerning work he has done with range data using argon as the test gas.

Figure 27 shows an oblique-view image-converter photograph of a Track G model under high-pressure conditions with no helium gas at this station (note the radiation visible from the shock cap).

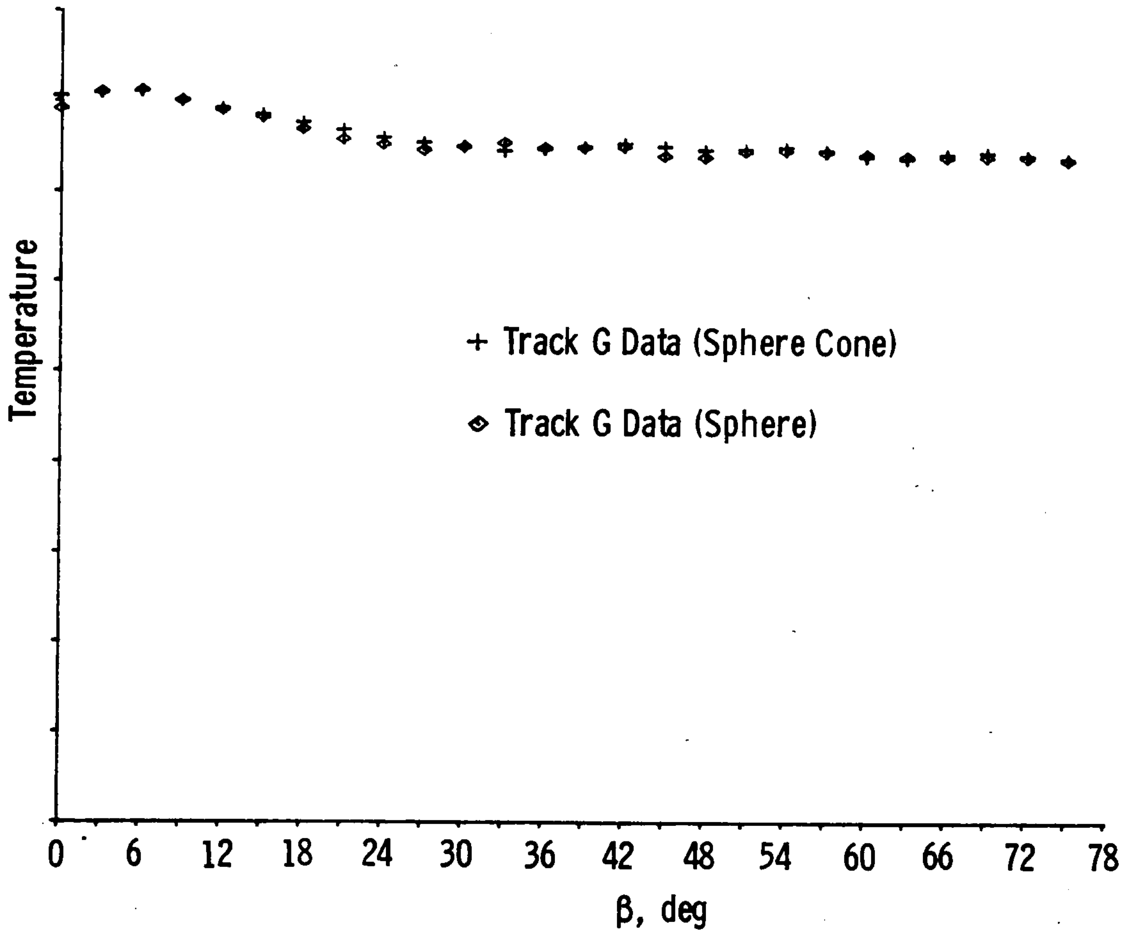

Figure 26. Effect on Temperature of Sphere Cone versus Sphere Options in Data Reduction Scheme.

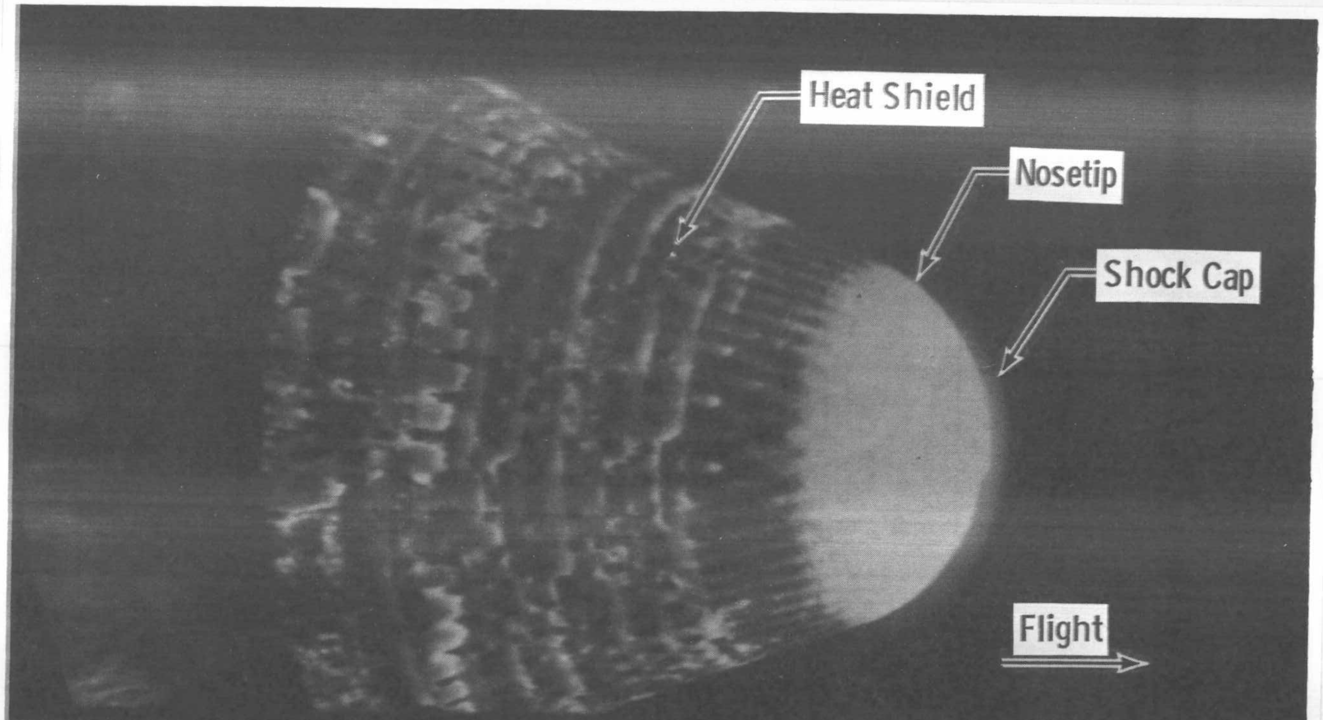

Figure 27. Image-Converter Photograph without Helium.

Figure 28 shows another Track G model with the nosetip from the same billet of material as it passes the same image-converter station. The range conditions are virtually identical. The only difference is the body heat-shield material (see Figure 8, page 13) and the fact that the helium gas is used on this shot to quench the shock cap.

The apparent material loss from the nosetip is similar on all image-converter photographs taken during this flight. Calculations of the dynamic pressure difference experienced by the model surface upon entry into the helium reveal a drop to about one-seventh the level in air. As many of the materials tested were porous by design, it is conceivable that an abrupt decrease in pressure on the surface could cause a material ejection (see Figure 28) as the gases expand to equalize pressure.

The ASCC-G predicts internal temperatures at each of the points shown within the model (see Figure 13, page 24) and predicts a very steep gradient at the surface throughout the model flight. A simple calculation was performed to determine how far into the model surface (at the stagnation point) one would have to go to reach temperatures equivalent to the measured surface temperature data. The resulting distance was on the order of the underprediction shown in Figure 18, page 32. This was the

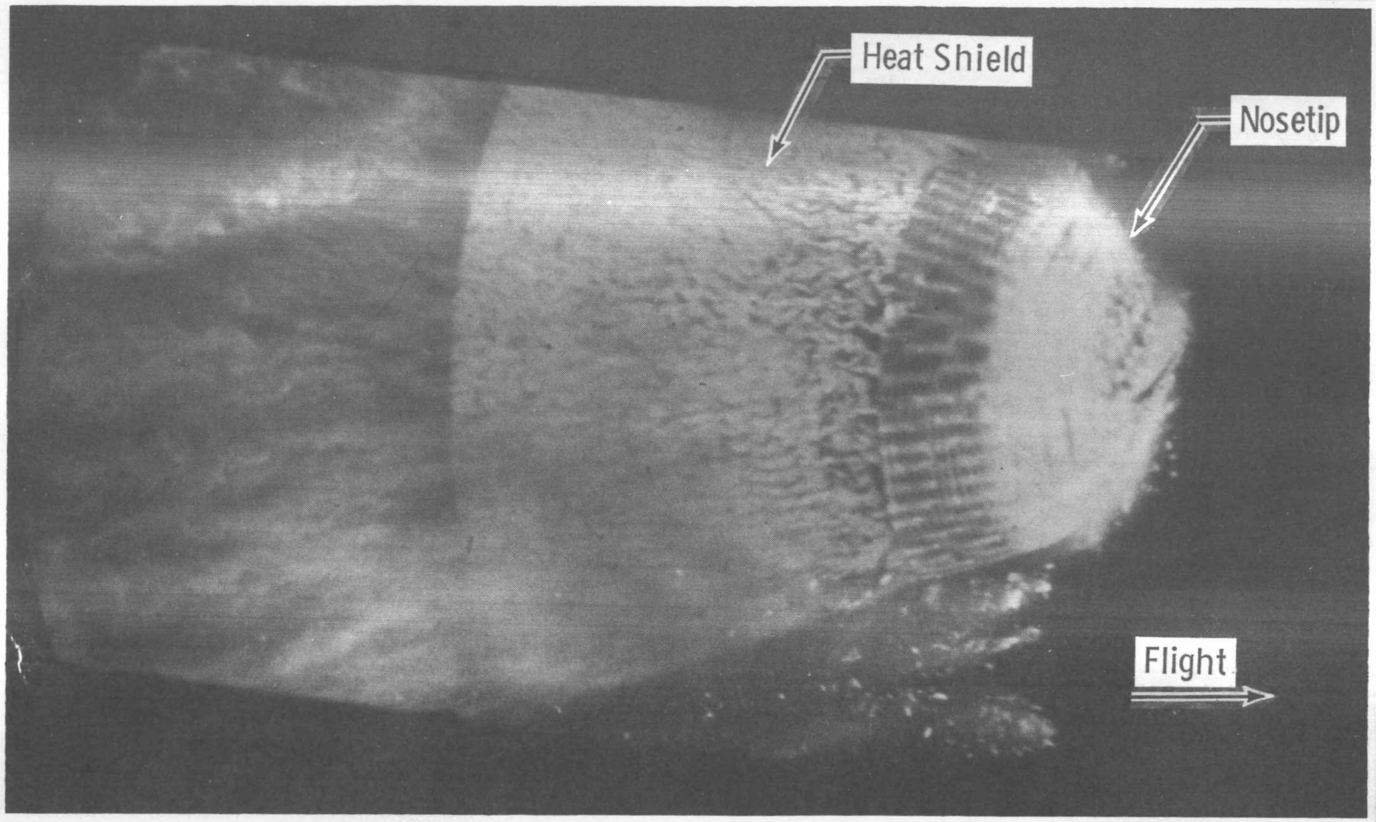

Figure 28. Image-Converter Photograph with Helium.

case in every shot studied at almost every IC station. Hence, the step decrease in dynamic pressure on the model (upon entering the helium environment) may result in more model recession than predicted, as shown in Figure 18, page 32, as well as a decrease in measured model surface temperature, because the hot surface is ejected and the cooler surface exposed just prior to the image-converter photograph. This possibility, as well as other potential error sources noted, are being investigated further at AEDC.

CHAPTER V

CONCLUSIONS

A relatively new testing technique involving pressurization of the AEDC Track G facility has been developed. Representative data, compared to the ASCC-G theoretical predictions, show good agreement on shock shape and location, but the code slightly underpredicts stagnation point recession and overpredicts model surface temperature by 30 to 50 percent. Several explanations are being investigated at this time, with the helium shock-cap quench effects being the most probable explanation.

Follow-on work might include stress analysis of a Track G model using the internal temperatures predicted by the ASCC-G as inputs along with the external pressure field just prior to and just after model exposure to the helium environment. If these computations seem to indicate material failure, then an estimate will be made of the pressure decrease tolerable and an alternate method suggested to quench the shock cap. Possibilities include the use of a gas of greater density than helium with similar chemiluminescence under the test conditions. Another avenue may be model preheating to lessen the thermal gradient within the model prior to the helium encounter.

BIBLIOGRAPHY

BIBLIOGRAPHY

1. Norfleet, G. D., R. E. Hendrix, and D. Jackson. "Development of a Hypervelocity Track Facility at AEDC." American Institute of Aeronautics and Astronautics Paper No. 77-151, presented at the Fifteenth Aerospace Sciences Meeting, Los Angeles, California, January 24-26, 1977.

2. Test Facilities Handbook. Eleventh edition. Vol. 3. Arnold Air Force Station, Tennessee: Arnold Engineering Development Center, 1981.

3. Dugger, P. H., C. P. Enis, and R. E. Hendrix. "Aeroballistics Range Photopyrometry," Arnold Engineering Development Center TR-82-1, Arnold Air Force Station, Tennessee, February 1982.

4. Eisenhart, C. "Expression of Uncertainties of Final Results, Precision Measurement and Calibration," National Bureau of Standards Handbook 91. Vol. I. National Bureau of Standards, United States Department of Commerce. Washington: Government Printing Office, 1969. Pp. 69-72.

5. Seigel, R., and J. R. Howel. Thermal Radiation Heat Transfer. New York: McGraw-Hill, 1972. P. 726.

6. Thompson, R. A., and C. H. Lewis. "Effects of Weather Encounters on Zero-Lift Reentry Vehicles." American Institute of Aeronautics and Astronautics Paper No. 82-0858, presented at the Third Joint Thermophysics Fluids, Plasma, and Heat Transfer Conference, St. Louis, Missouri, June 7-11, 1982.

7. Reda, D. C. "Correlation of Nosetip Boundary-Layer Transition Data Measured in Ballistic-Range Experiments," Sandia Laboratories SAND-79-0649, Albuquerque, New Mexico, November 1979.

8. Powers, C. A., and R. M. Kendall. "User's Manual: Aerotherm Chemical Equilibrium (ACE) Computer Program," Aerotherm Corporation, Mountain View, California, May 1969.

9. Reynolds, M. M., R. J. Corruccini, M. M. Fulk, and R. M. Burley. "Radiometry," American Institute of Physics Handbook, Dwight E. Gray, editor. New York: McGraw-Hill, 1963. Pp. 6-153.

10. Kratsch, K. M., M. R. Martinez, F. I. Clayton, R. B. Greene, and J. E. Wuerer. "Graphite Ablation in High-Pressure Environments." American Institute of Aeronautics and Astronautics Paper No. 68-1153, presented at the Entry Vehicle Systems and Technology Meeting, Williamsburg, Virginia, December 3-5, 1968.

11. Park, C. "Stagnation-Point Ablation of Carbonaceous Flat Disks in an Argon-Filled Ballistic Range. Part 2. Experiment," American Institute of Aeronautics and Astronautics Journal, 21:1748-1754, December 1983.

VITA

The author, Jere J. Matty, was born on February 28, 1956, in Denver, Colorado. He attended elementary schools in that city and in Anaheim, California. His family moved to Chesapeake, Virginia, where he attended high school. Upon graduation he accepted an appointment to the USAF Academy, Colorado, where he graduated in 1978 with a Bachelor of Science degree in Aeronautical Engineering. In 1981 he entered the graduate program at The University of Tennessee Space Institute on a part-time basis and was awarded the Master of Science degree in Mechanical Engineering in June 1984. He serves in the Air Force as a pilot and engineer.

The author is married to the former Rosemary Ricohermoso of Chesapeake, Virginia. They reside in Tullahoma, Tennessee, with their two children, Christopher and Tina.